

RECOVERING INTERSTELLAR CLOUDS WITH HI SPECTRAL LINES: A COMPARISON BETWEEN SYNTHETIC OBSERVATIONS AND 21-SPONGE

CLAIRE E. MURRAY^{1†}, SNEŽANA STANIMIROVIĆ¹, CHANG-GOO KIM², EVE C. OSTRIKER², ROBERT R. LINDNER¹, CARL HEILES³, JOHN M. DICKEY⁴, BRIAN BABLER¹

Draft version December 9, 2024

ABSTRACT

We analyze synthetic neutral hydrogen (HI) absorption and emission spectral lines from a high-resolution, three-dimensional hydrodynamical simulation to quantify how well observational methods recover physical properties of interstellar clouds. We present a new method for uniformly decomposing HI spectral lines and estimating the properties of associated clouds using the Autonomous Gaussian Decomposition (AGD) algorithm. We find that HI spectral lines recover clouds with excellent completeness at high Galactic latitude, and this completeness declines with decreasing latitude due to strong velocity-blending of spectral lines. The temperature and column density inferred from our decomposition and radiative transfer method agree with the simulated values within a factor of < 2 for the majority of clouds. We next compare synthetic spectra with observations from the 21-SPONGE survey at the Karl G. Jansky Very Large Array using AGD. We find more components per line of sight in 21-SPONGE than in synthetic spectra, which reflects insufficient simulated gas scale heights and the limitations of local box simulations. In addition, we find a significant population of low-optical depth, broad absorption components in simulations which are not seen in 21-SPONGE. This population is not obvious in integrated or per-channel diagnostics, and reflects the benefit of studying velocity-resolved components. In addition, the discrepant components correspond to the highest spin temperatures ($1000 < T_s < 4000$ K), which are not seen in 21-SPONGE despite sufficient observational sensitivity. We demonstrate that our analysis method is a powerful tool for diagnosing neutral ISM conditions, and future work is needed to improve observational statistics and implementation of simulated physics.

1. INTRODUCTION

Neutral hydrogen (HI) in the interstellar medium (ISM) plays a crucial role in the life cycles of galaxies. The atomic medium provides the main fuel reservoir for molecular gas and, ultimately, star formation. Furthermore, the structure of interstellar HI bears important clues to the nature of gas recycling via radiative and dynamical feedback and Galactic winds (e.g., McClure-Griffiths et al. 2015).

Throughout the ISM, HI exists in a “multi-phase” state. This structure is characterized by two thermally-stable phases in pressure equilibrium (Field et al. 1969; McKee & Ostriker 1977; Wolfire et al. 2003): the cold neutral medium (CNM) and warm neutral medium (WNM). An effective constraining observable for the balance between the CNM and WNM is the excitation temperature (a.k.a., spin temperature, T_s) of the gas. However, both emission and absorption by the 21 cm hyperfine transition of HI are required to measure T_s . Therefore, although the CNM ($T_s \sim 20 - 200$ K) as been extensively analyzed with HI absorption (e.g., Crovisier et al. 1978; Dickey et al. 2003; Heiles & Troland 2003a), excellent sensitivity is required to constrain the temperature

of the WNM ($T_s \sim 1000 - 7000$ K), and few measurements exist (Carilli et al. 1998; Dwarakanath et al. 2002; Roy et al. 2013; Murray et al. 2014, 2015).

To understand the physical mechanisms responsible for observed HI properties, comparisons between observations and theory are necessary. Synthetic observations of numerical simulations provide a means to directly compare real observations with applied theory. For example, the velocity structures of synthetic spectral lines provide important diagnostics of interstellar turbulence (e.g., Falgarone et al. 1994), and the nature of CNM cloud dynamics (Hennebelle et al. 2007; Saury et al. 2014). Furthermore, synthetic observations have been used extensively to investigate molecule formation (Shetty et al. 2011; Smith et al. 2014; Duarte-Cabral et al. 2015; Duarte-Cabral & Dobbs 2016) and Galactic morphology (Douglas et al. 2010; Acreman et al. 2012; Pettitt et al. 2014). Important observational biases can be directly quantified using these comparisons. In particular, considering correspondence between the true positions and observed velocities of molecular clouds, Beaumont et al. (2013) showed that the superposition of clouds along the line of sight introduces significant uncertainty to observational estimates of cloud mass, size and velocity dispersion.

However, numerical simulations with suitable dynamic range and resolution for describing the dynamics of both the CNM and WNM have only recently been performed. Kim et al. (2014) constructed a sample of synthetic HI absorption and emission spectral lines from their three-dimensional hydrodynamical simulations (Kim et al. 2013). Comparing true simulated conditions with properties inferred from synthetic observa-

¹ Department of Astronomy, University of Wisconsin, Madison, WI 53706, USA

² Department of Astrophysical Sciences, Princeton University, Princeton, NJ 08544, USA

³ Radio Astronomy Lab, UC Berkeley, 601 Campbell Hall, Berkeley CA 94720, USA

⁴ University of Tasmania, School of Maths and Physics, Hobart, TAS 7001, Australia

† cmurray@astro.wisc.edu

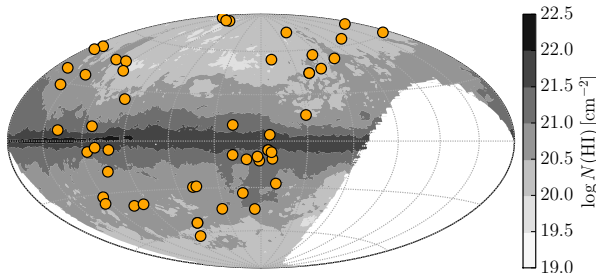


FIG. 1.— Galactic HI column density ($N(\text{HI})$) map from the Leiden Dwingeloo Survey. The locations of the 52 21-SPONGE HI absorption line sources are overlaid.

tions, Kim et al. (2014) found excellent agreement between “true” and “observed” per-channel and line of sight (LOS)-integrated properties such as column density and spin temperature. Furthermore, they showed that column densities computed in the optically-thin limit significantly underestimate the true column density when the HI optical depth is greater than $\tau \sim 1$. This agrees with previous comparisons of observed and simulated LOS column density by Chengalur et al. (2013), who constructed a two-phase medium by hand to test the role of optically-thick HI. However, Kim et al. (2014) found the discrepancy factor to be much smaller than Chengalur et al. (2013), indicating that when proper dynamics are considered, spectral line blending due to overlapping cold clouds is not significant.

Although LOS-integrated ISM properties provide important diagnostics, they correspond to physical quantities only in the case of a single-temperature medium along the LOS. Observations show that even high galactic latitude lines of sight contain several clouds of varying spin temperature (e.g., Heiles & Troland 2003a; Begum et al. 2010; Roy et al. 2013; Murray et al. 2015). The technique of Gaussian decomposition is one method that can identify individual spectral components from disparate HI phases, and has been used extensively to disentangle complex spectral lines (e.g., Lazareff 1975; Mebold et al. 1982; Dickey & Lockman 1990; Mohan et al. 2004). When applied to both HI absorption and emission spectra, Gaussian decomposition can be used to estimate the spin temperatures of individual clouds and the fraction of CNM along the line of sight (Heiles & Troland 2003a; Stanimirović et al. 2014; Murray et al. 2015). However, the method suffers from non-uniqueness complications, as Gaussian functions do not form an orthogonal basis (e.g., Heiles & Troland 2003a) and the number of Gaussian functions used to produce reasonable spectral fits can vary significantly. For example, comparing the Gaussian decompositions of the Galactic HI absorption spectrum towards 3C138, there are no fitted components which agree between the 6 found by Murray et al. (2015) and the 13 found by Roy et al. (2013). Furthermore, no quantitative estimates of how well Gaussian functions recover true properties of interstellar clouds exist.

Our paper is motivated by two goals. The first is to quantify how well Gaussian analysis of HI spectral lines

recovers true interstellar cloud properties. We compare “observed” and “true” cloud properties using 1000s of synthetic observations from 3D hydrodynamical simulations from Kim et al. (2013, 2014). To analyze synthetic observations, we use the Autonomous Gaussian Decomposition (AGD) algorithm (Lindner et al. 2015). AGD implements derivative-based computer vision to perform Gaussian decomposition of spectral lines, enabling efficient, reproducible and objective fits.

The second goal of this paper is to compare synthetic and real HI observations objectively using AGD. We use data from the 21-cm Spectral Line Observations of Neutral Gas with the VLA (21-SPONGE) survey, one of the largest, most sensitive Galactic 21 cm surveys (Murray et al. 2015), for comparison with the Kim et al. synthetic HI spectra. We aim to determine whether the influence of simulated feedback mechanisms on the properties and phase balance of CNM and WNM traced by real and synthetic observations can be resolved by observational analysis methods.

In Section 2, we describe the 21-SPONGE observations, and in Section 3 we describe Kim et al. simulations and synthetic observations. We present and discuss our Gaussian analysis method in Section 4. In Section 5, we compare the properties of clouds from synthetic observations with the true properties of clouds from the simulated LOS. We then compare the synthetic observations with 21-SPONGE observations in Section 6. Finally, we present our summary and conclusions in Section 7.

2. OBSERVATIONS

For observations of Galactic HI, we use data from the 21-SPONGE survey (Murray et al. 2015). 21-SPONGE is the largest, most sensitive survey of Galactic HI absorption at the Karl G. Jansky Very Large Array (VLA) to date. We target strong extragalactic radio continuum sources mostly at high Galactic latitudes ($|b| > 5^\circ$), and consistently reach RMS noise in HI optical depth of $\sigma_\tau < 10^{-3}$ per 0.4 km s^{-1} channels.

21-SPONGE utilizes HI emission observations along the same LOS from the Arecibo Observatory ($\sim 3.5'$ beam at 21 cm). The emission spectrum in the direction of each source is computed by observing a pattern of 16 off-source positions and interpolating across the target position (see, e.g., Heiles & Troland 2003a, hereafter HT03). We note that the Arecibo HI emission profiles are not corrected for an effect known as “stray radiation”, wherein radiation enters the main telescope beam through higher-order side lobes. Although stray radiation can be modeled and removed from HI emission data (e.g., LAB and GASS surveys; Kalberla et al. 2005; McClure-Griffiths et al. 2009), it is a complex process requiring stable beam shapes which are not achieved at Arecibo. The effect is only significant for emission, not absorption, and typically contributes $\lesssim 1 \text{ K}$ over 50 km s^{-1} to the brightness temperature. In addition, stray radiation is not very important at Galactic latitudes below $\sim 60^\circ$.

Armed with high-sensitivity HI absorption and emission spectra along each line of sight, 21-SPONGE is sensitive to HI column densities and temperatures from all neutral ISM phases, including the CNM, WNM and thermally unstable medium.

In Murray et al. (2015), we presented the survey

design, analysis methods and initial results for 21-SPONGE. To derive physical properties of clouds along each line of sight, we decomposed (by hand) HI absorption and emission spectral pairs simultaneously into Gaussian functions, and solved radiative transfer equations to derive the column density and temperature of individual spectral components, taking into account the presence of self-absorption and the order of clouds along each line of sight (as done, e.g., in HT03, Stanimirović & Heiles 2005; Stanimirović et al. 2014). We found excellent agreement with previous HI absorption surveys. The high sensitivity of 21-SPONGE allowed us to extend the maximum HI spin temperatures detected directly in absorption and emission from 600 K in HT03 to ~ 1500 K (Murray et al. 2015).

Figure 1 displays the positions of the 52 21-SPONGE sources overlaid on an HI column density map from the Leiden Dwingeloo Survey (LDS; Hartmann & Burton 1997). The targets probe a large range in Galactic latitude.

3. NUMERICAL SIMULATIONS

For simulations of interstellar HI, we use recent high-resolution Galactic ISM simulations by Kim et al. (2013, hereafter KOK13). These simulations include momentum feedback from supernovae, time-varying heating, interstellar cooling, galactic differential rotation, gaseous self-gravity and external gravity from dark matter and stars. We refer the reader to KOK13 for a full description of their setup, methods and evolution.

Using these simulations, Kim et al. (2014, hereafter KOK14) constructed a set of synthetic spectral line observations of the local ISM. Assuming an observer sits in the center of the simulation, they selected 10^4 positions randomly distributed in Galactic latitude (l) and longitude (b) and extracted the number density (n), temperature (kinetic, T_k , and spin, T_s) and velocity (v) as functions of path length (s). These lines of sight (LOS) are restricted to $|b| > 4.9^\circ$ and $s \leq 3$ kpc so that the limited horizontal extent of the simulation does not adversely affect the results, as would be a concern at low Galactic latitude. For the particular KOK13 simulation we analyze in this work (QA10), galactic rotation was applied with assumed angular velocity of $\Omega = 28$ km sec $^{-1}$ and gas surface density $\Sigma = 10 M_\odot$ pc $^{-2}$ (KOK13).

For each observed LOS, KOK14 produced synthetic HI emission and absorption as functions of radial velocity using analytical radiative transfer and HI excitation prescriptions. The reader is referred to Section 2.3 of KOK14 for a complete description of the methods used to construct the synthetic observations.

In particular, as part of their model for synthetic 21 cm level populations, KOK14 considered indirect radiative transitions due to resonant scattering by Ly α photons (the Wouthuysen-Field (WF) effect; Wouthuysen 1952; Field 1959) in addition to collisions and direct radiative transitions. They parameterized the WF effect following Field (1959) with a constant value for the Galactic Ly α photon number density, n_α , inferred from Liszt (2001) to be $n_\alpha = 10^{-6}$ cm $^{-3}$. This value of n_α is highly uncertain and difficult to constrain observationally or numerically. Given that observed LOS-integrated and per-channel properties are dominated by high-optical depth gas, wherein the 21 cm transition is already thermalized

by collisions due to high densities, the WF effect does not significantly affect these values. The WF effect should be most important for the WNM, where generally $T_s \leq T_k$ due to the inefficiency of collisions at thermalizing the 21 cm transition (e.g., Liszt 2001). Indeed, at high T_s the effect is significant (c.f., Figures 9a, 10a of KOK14).

We note that the KOK13 simulations do not include chemistry and the HI-to-H $_2$ conversion. In addition, their implemented supernova feedback injects momentum and not thermal energy, resulting in the absence of a hot ($T \sim 10^5 - 10^6$ K) medium. Although these are secondary effects, and they are being addressed in ongoing simulations (Kim et al., in preparation), we need to keep this in mind when considering properties of synthetic observations from KOK14.

In this paper, we analyze components within the synthetic KOK14 HI spectral pairs to investigate how radiative transfer-based Gaussian fitting reproduces real physical quantities. From their catalog of 10^4 spectral pairs, we selected those without saturated (defined here as $\tau \geq 3$) or NaN-valued absorption lines, for a final catalog of 9355 HI spectral pairs. To simulate observational conditions, we added Gaussian-distributed noise with an amplitude of $\sigma_\tau = 10^{-3}$ to each absorption spectrum (equal to the median RMS noise in τ per channel from 21-SPONGE) and $\sigma_{T_B} = 0.2$ K to each emission spectrum (equal to the median RMS noise in T_B per channel in 21-SPONGE).

4. GAUSSIAN DECOMPOSITION WITH AGD

To perform Gaussian fits to HI spectra, we use the Autonomous Gaussian Decomposition algorithm (AGD; Lindner et al. 2015). AGD implements derivative spectroscopy and machine learning techniques to efficiently and objectively provide initial guesses (i.e., amplitude, width, mean velocity) for multiple-Gaussian fits to spectral line data.

Before implementing AGD, we trained the algorithm to maximize the decomposition accuracy. We began by constructing a synthetic HI dataset from the Gaussian components detected by the Millennium Arecibo 21 cm Absorption Line Survey (HT03, Heiles & Troland 2003b). The synthetic training dataset construction and training are described fully in Lindner et al. (2015), and summarized here for clarity. We selected the number of components in each synthetic spectrum to be a uniform random integer ranging from the mean number of components in the survey (3) to the maximum number (8; HT03), and then drew the component parameters from the published HT03 amplitude, FWHM and mean velocity distributions from with replacement. As done with the KOK14 synthetic spectra, we added Gaussian-distributed noise with an amplitude of $\sigma_\tau = 10^{-3}$ to each absorption spectrum (equal to the median RMS noise in τ per channel from 21-SPONGE) and $\sigma_{T_B} = 0.2$ K to each emission spectrum (equal to the median RMS noise in T_B per channel in 21-SPONGE). The synthetic training sets for absorption and emission consist of 20 spectra each.

After constructing the synthetic training dataset, we used the python implementation of AGD, GaussPy, to decompose the synthetic training dataset for different values of the “two-phase” smoothing parameters α_1 and α_2 . These smoothing parameters serve to identify the types of spectral properties present in the data. Begin-

TABLE 1
AGD SUMMARY

Source	LOS	Absorption		Emission		Matched ^b	
	(number)	(number)	(per LOS) ^a	(number)	(per LOS) ^a	(number)	(per LOS) ^a
KOK14	9355	14023	1.5 ± 1.7	23475	2.5 ± 1.4	9218	1.0 ± 1.1
KOK14 (no WF)	9355	15468	1.7 ± 1.8	23519	2.5 ± 1.4	9490	1.0 ± 1.1
21-SPONGE	52	237	4.6 ± 3.0	326	6.3 ± 2.9	88	1.7 ± 1.3

^a: Mean and standard deviation over all LOS

^b: “Matched” statistics will be discussed in Section 6.

ning with initial choices for α_1 and α_2 and a signal-to-noise (S/N) threshold below which the algorithm will not select components (S/N=3.0), GaussPy computes the accuracy of the decomposition (i.e. how closely the derived model parameters are to the true model parameters), for iteratively different values of α_1 and α_2 until it converges on minimal model residuals and maximum decomposition accuracy. After training, we found accuracies of 80% and 70% for HI absorption and emission decompositions, respectively. The resulting values are $\alpha_1 = 1.12$ and $\alpha_2 = 2.73$ for absorption and $\alpha_1 = 1.70$ and $\alpha_2 = 3.75$ for emission.

With trained values of α_1 and α_2 in hand, we used GaussPy to apply the AGD algorithm identically (i.e. same values of α_1 , α_2 and S/N) to the observed 21-SPONGE and simulated KOK14 spectra to derive lists of Gaussian parameters for each dataset. Table 1 summarizes the decomposition results for the emission and absorption spectra from 21-SPONGE and KOK14 including the WF effect and without the WF effect (“no WF”). The typical uncertainties in the fitted parameters are $\sim 1 - 10\%$ from the least-squares fit applied by AGD.

5. QUANTIFYING THE ACCURACY OF THE GAUSSIAN-FITTING METHOD WITH SYNTHETIC OBSERVATIONS

From the KOK14 simulations, we have information about the density and temperature as a function of distance ($n(s)$, $T(s)$), as well as the optical depth and brightness temperature as a function of velocity ($\tau(v)$, $T_B(v)$) for each line of sight. Therefore, following AGD analysis, we can compare observed properties of spectral lines to the true properties of simulated clouds. This will allow us to quantify the biases and limitations of Gaussian analysis in reproducing realistic physical properties.

5.1. Defining clouds in position and velocity

Given that $\tau \propto n/T_s$, we define density structures (or clouds) by selecting peaks in n/T_s along each LOS. To select a threshold value, we consider the parameters of the simulated ISM from KOK13. The gas temperature and density PDFs in their Figure 8 display strong bi-modality indicative of multiple HI phases. We select $n \sim 2 \text{ cm}^{-3}$ and $T \sim 10^3 \text{ K}$ as representative values between the peaks of the published bi-modal PDFs (KOK13). These values correspond to a threshold of $(n/T_s)_{\text{thresh}} = 0.002 \text{ cm}^{-3}/\text{K}$. We experimented with different values of this threshold, and the subsequent results do not change significantly.

In Figure 2, we display $(n/T_s)(s)$ (left), $\tau(v)$ (middle) and $T_B(v)$ (right) for 5 example LOS from KOK14. The positions of clouds above $(n/T_s)_{\text{thresh}} = 0.002 \text{ cm}^{-3}/\text{K}$ are plotted as colored circles. Across all 9355 synthetic LOS, there are 7582 clouds with $(n/T_s) > 0.002 \text{ cm}^{-3}/\text{K}$.

To compare the properties of simulated clouds with synthetic spectral lines, we first determine the position and line width of each cloud as a function of velocity. We define the “velocity” of each cloud, v_{sim} , by computing the average velocity ($v(s)$) of channels spanned by each cloud weighted by their densities ($n(s)$), specifically,

$$v_{\text{sim}} = \frac{\int_{\text{cloud}} n(s) v(s) ds}{\int_{\text{cloud}} n(s) ds}, \quad (1)$$

where “cloud” refers to all pixels spanned by each cloud above $(n/T_s)_{\text{thresh}} = 0.002 \text{ cm}^{-3}/\text{K}$. These values are plotted in the middle and right columns of Figure 2 as circles with colors corresponding to the labels in the left column (n/T_s). Next, we estimate the FWHM of the cloud in velocity simply by considering the thermal contributions. We compute the simulated line width, Δv_{sim} , by solving (e.g., Eq. 9.31, Draine 2011),

$$\Delta v_{\text{sim}} = 1.90 \sqrt{T_{\text{mean}}/100 \text{ K}}. \quad (2)$$

with an assumed mean molecular weight of $\mu = 1.27$, where T_{mean} is the harmonic mean kinetic temperature of the gas spanned by each cloud, given by,

$$T_{\text{mean}} = \frac{\int_{\text{cloud}} n(s) ds}{\int_{\text{cloud}} (n/T)(s) ds}. \quad (3)$$

The values of Δv_{sim} lie between $\sim 1 - 10 \text{ km s}^{-1}$ for a range of density threshold choices.

5.2. Matching clouds with HI absorption lines

To match AGD-fitted Gaussian absorption lines with clouds along each LOS, we use two matching criteria. First, we define δ_v to be the difference in mean velocity of a component fitted in absorption (v_0) with the simulated velocity of the cloud (v_{sim}) in terms of the measured FWHM from the fit in absorption (Δv_0), or,

$$\delta_v \equiv \frac{|v_0 - v_{\text{sim}}|}{\Delta v_0/2.355}, \quad (4)$$

For a cloud to match a component, we require that their positions in velocity space be less than one standard deviation away from each other, so that,

$$\delta_v \leq 1. \quad (5)$$

Second, we define δ_{FWHM} to be the ratio of the FWHM of a component in absorption (Δv_0) and the estimated FWHM of the cloud in velocity (Δv_{sim}), or,

$$\delta_{\text{FWHM}} \equiv \Delta v_{\text{sim}}/\Delta v_0. \quad (6)$$

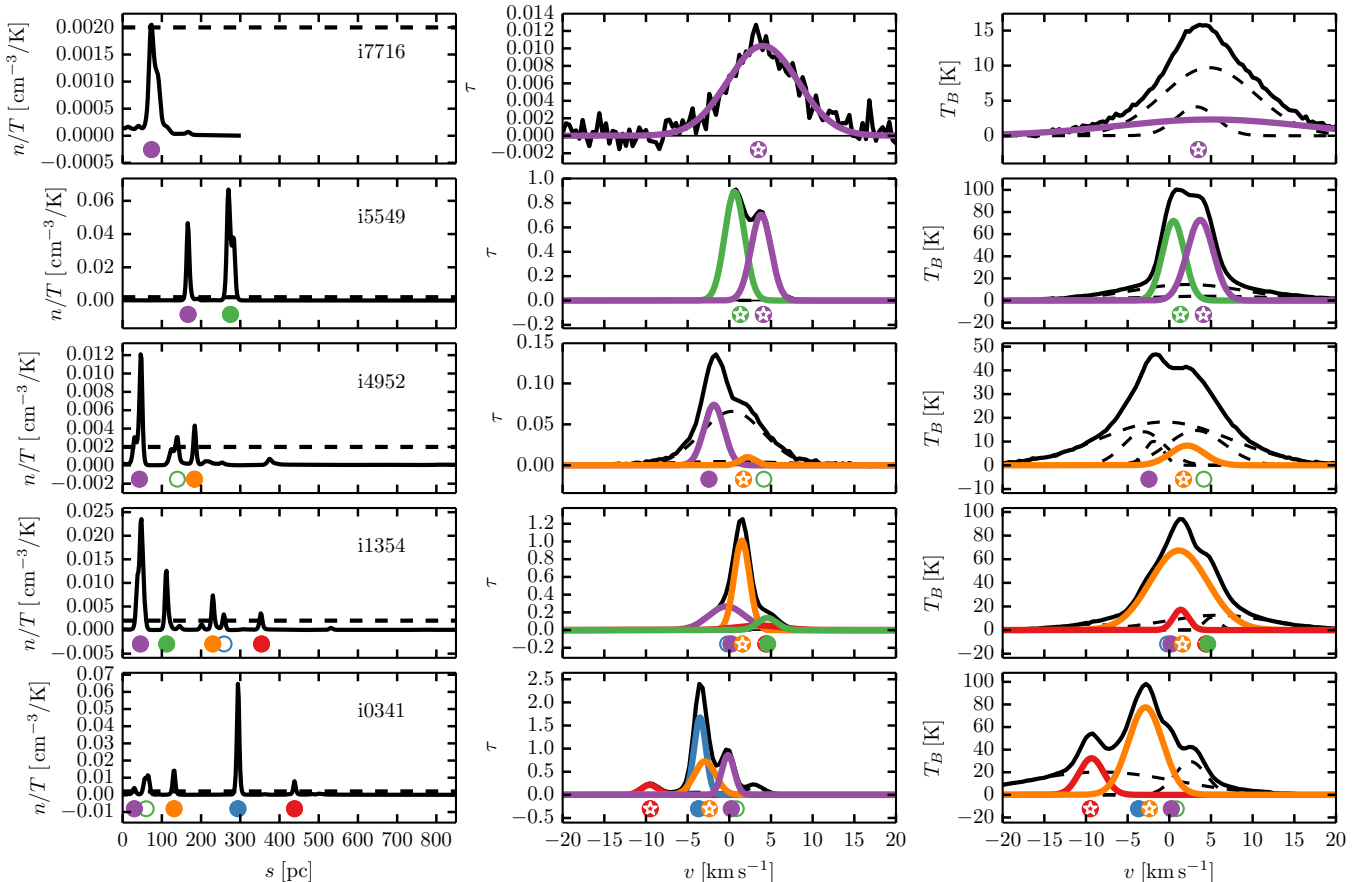


FIG. 2.— Example LOS from KOK14. Left: density over gas temperature (n/T_s) as a function of distance (s) along the LOS; Middle: synthetic optical depth as a function of velocity ($\tau(v)$); Right: synthetic brightness temperature as a function of velocity ($T_B(v)$). Clouds defined by peaks above $(n/T_s)_{\text{thresh}} = 0.002 \text{ cm}^{-3}/\text{K}$ are indicated by colored circles in each panel. If the cloud matches with an AGD absorption line according to Equations 5 and 7, the circles are filled and the matching AGD absorption line is plotted in the corresponding color. If the cloud matches with an AGD emission line according to Equations 8 and 9, the circle symbol has a white star within it.

To determine a limit for δ_{FWHM} , we consider the line-broadening due to turbulent conditions in the medium. The turbulent Mach number, M_t , is a measure of how strongly non-thermal, turbulent motions contribute to the line width, and is given by, $M_t^2 = v_{\text{turb}}^2/c_s^2$, where v_{turb} is the turbulent velocity and c_s is the sound speed in the medium. We use the typical value of M_t in the CNM, or $M_t = 3$ (e.g., Heiles & Troland 2003b, Murray et al. 2015) to set a limit to the ratio of FWHM or,

$$\delta_{\text{FWHM}} \leq 3. \quad (7)$$

We note that choices of cutoff value for δ_{FWHM} between 1 and 5 does not significantly change the results, as the criterion described by Equation 8 dominates the matching.

In Figure 2, the circle markers for clouds which match with AGD absorption lines according to Equations 5 and 7, are filled, and the matching AGD absorption line is plotted in the corresponding color in the middle panel. If a cloud does not have an AGD match, the circle marker is unfilled. Of the 7582 total clouds, there are 6311 clouds with matches to AGD absorption lines.

5.2.1. Matching absorption with emission

Both HI absorption ($\tau(v)$) and emission ($T_B(v)$) information are required to constrain the spin temperature (T_s) and column density ($N(\text{HI})$) of neutral gas clouds in the ISM. Therefore, to compare the true density and temperature of simulated clouds with properties inferred from observations, we need to determine the optical depth *and* brightness temperature of each cloud.

To match HI absorption lines with HI emission lines fitted by AGD, we apply a similar set of match criteria as described by Equations 5 and 7. Specifically,

$$\delta_{v,\text{AGD}} \equiv \frac{|v_0 - v_{0,\text{em}}|}{\Delta v_0/2.355} \leq 1, \quad (8)$$

$$1 \leq \delta_{\text{FWHM,AGD}} \equiv \Delta v_{0,\text{em}}/\Delta v_0 \leq 3, \quad (9)$$

where $(v_0, \text{em}, \Delta v_{0,\text{em}})$ are the mean velocity and FWHM of an AGD component fitted to $T_B(v)$. We impose the requirement that $\delta_{\text{FWHM,AGD}} \geq 1$ to ensure that the matched line width is larger in emission than absorption.

In Figure 2, if a cloud (left panel) matches with an AGD absorption line (middle panel) and also matches with an AGD emission line (right panel) according to Equations 8 and 9, the circle marker contains a white star and the matching emission line is plotted in the corresponding color (right panel). Of the 6311 clouds with

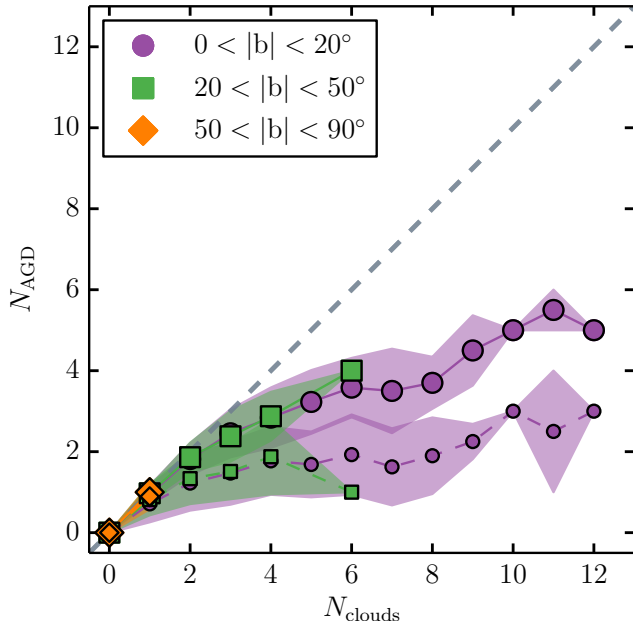


FIG. 3.— The number of clouds defined by $n/T_s > 0.002 \text{ cm}^{-3}/\text{K}$ along a synthetic LOS (N_{clouds}) compared with the number of AGD-fitted lines (N_{AGD}). Large symbols show N_{AGD} matched in absorption according to Equations 5 and 7, and small symbols show N_{AGD} matched in absorption and emission according to Equations 5, 7, 8 and 9. Symbols and shading indicate the mean and standard deviations of N_{AGD} for each unique N_{clouds} . The samples are binned by latitude according to the inset legend.

AGD absorption line matches, 4337 clouds also have a match to an AGD emission line.

5.3. Quantifying Match Completeness

In Figure 3 we compare the number of clouds (N_{clouds}) along each synthetic LOS with the number of matched AGD-fitted lines (N_{AGD}). For each unique value of N_{cloud} , the mean (symbol) and standard deviation (shading) of N_{AGD} are shown. Furthermore, we break the sample into latitude bins according to the inset legend. Large symbols indicate the number of AGD absorption matches according Equations 5 and 7, and small symbols indicate the number of AGD absorption *and* emission matches following the subsequent application of Equations 8 and 9.

Using Figure 3, we quantify the completeness (C) of cloud recovery by,

$$C = \frac{\sum N_{\text{AGD}}}{\sum N_{\text{clouds}}}. \quad (10)$$

For the matches between clouds and absorption lines only (large symbols), the completeness for the low ($0 < |b| < 20^\circ$), mid ($20 < |b| < 50^\circ$) and high latitude ($|b| > 50^\circ$) bins are $C_{\text{absorption}} = (0.54, 0.76, 1.00)$ respectively. The recovery is best at the highest latitudes where the number of clouds and AGD lines are smallest and the LOS complexity is minimized, allowing for simple and robust AGD fits. At low latitudes, the blending of clouds and AGD components makes it difficult to associate unambiguous spectral components with (n/T_s) peaks.

When matching clouds to HI emission instead of absorption, the recovery completeness is $C_{\text{emission}} = (0.42, 0.51, 0.93)$ for low, mid and high latitudes respectively. The completeness is worse in emission than absorption, which reflects the increased complexity of fitting multiphase HI in emission. As observed in Figure 3, broad components associated with high-temperature HI are prominent, thereby making the match to corresponding clouds (defined as peaks in τ) more difficult. Although Gaussian analysis has been used extensively in the past to identify gas populations, this is among the first statistical quantification of the correspondence between HI emission components and interstellar clouds.

When matching clouds to both absorption and emission (small symbols in Figure 3), the completeness for the low, mid and high latitude bins are: $C_{\text{both}} = (0.29, 0.41, 0.89)$ respectively. At all latitudes, the cloud recovery completeness declines when the match between absorption and emission is performed. The bottom row of Figure 2 displays an example of this decline. Whereas 4/5 clouds along the LOS are recovered by AGD absorption lines, only 2/4 of those absorption lines have matches in emission according to Equations 8 and 9. The clouds selected by the matching process with both absorption and emission are biased towards unambiguous features in all three spaces. Nevertheless, the completeness of Gaussian decomposition for the multi-phase clouds seen in both emission and absorption is excellent at $|b| > 50^\circ$. This is certainly promising for future large data sets — even with $\sim 50\%$ attrition a large number of clouds can be retrieved over a wide range of interstellar conditions.

5.4. Observed vs. True Cloud Properties

Given a sample of clouds with matches to AGD components in absorption and emission, we compare the true simulated temperatures with the observed values.

5.4.1. Spin Temperature

With the goal of estimating spin temperature automatically for a large number of spectra, we take a more simplified approach than what has been done in HT03 or Murray et al. (2015). For each AGD match between absorption and emission, we start with the isothermal spin temperature as a function of velocity, $T_{s,\text{AGD}}(v)$, given by,

$$T_{s,\text{AGD}}(v) = \frac{T_{B,\text{AGD}}(v)}{1 - e^{-\tau_{\text{AGD}}(v)}}, \quad (11)$$

where $T_{B,\text{AGD}}(v)$ and $\tau_{\text{AGD}}(v)$ are the matched set of Gaussian functions fitted by AGD to $T_B(v)$ and $\tau(v)$ respectively. This method assumes a single temperature gas within each velocity channel. To estimate average spin temperature per AGD component, we compute the optical depth-weighted spin temperature per component,

$$T_{s,\text{AGD}} \equiv \frac{\int \tau_{\text{AGD}}(v) T_{s,\text{AGD}}(v) dv}{\int \tau_{\text{AGD}}(v) dv}. \quad (12)$$

This approach produces a weighted mean temperature for each component, given that $T_{s,\text{AGD}}(v)$ is smaller near the peak of $\tau_{\text{AGD}}(v)$ and larger away from it. There are several possible ways to estimate mean temperature from observations, and some discussion of the pros and

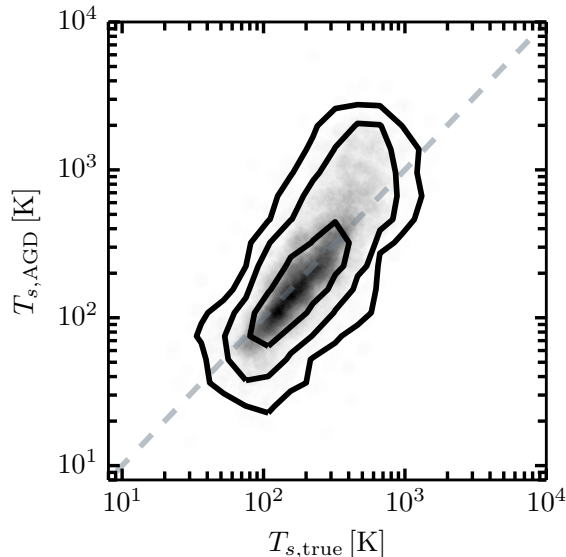


FIG. 4.— True, simulated spin temperature ($T_{s,\text{true}}$, Equation 13) versus observed spin temperature ($T_{s,\text{AGD}}$, Equation 12) for all clouds which match fitted absorption and emission lines according to Equations 5, 7, 8 and 9. Contours indicate the 1, 2 and 3 σ limits.

cons of each method are given in HT03 and Dickey et al. (2003). It is important to note that Equation 12 works well if, within a multi-phase cloud, the CNM and WNM are centered at a similar radial velocity. However, if the CNM is shifted in velocity relative to the WNM due to turbulent motions, so that the peaks of $T_{B,\text{AGD}}(v)$ and $\tau_{\text{AGD}}(v)$ are slightly offset, Equation 12 will overestimate $T_{s,\text{AGD}}$. HT03 and Murray et al. (2015) have allowed for the CNM motion relative to the WNM in their temperature estimates by using a more complex fitting approach where spin temperature is fitted simultaneously with all WNM components. This is, however, computationally expensive for us to implement at this stage.

To estimate the true temperature of a simulated cloud, we compute the harmonic mean temperature, $T_{s,\text{true}}$, within the pixels spanned by each cloud in n/T_s -space. Specifically,

$$T_{s,\text{true}} = \frac{\int_{\text{cloud}} n(s) ds}{\int_{\text{cloud}} (n/T_s)(s) ds}, \quad (13)$$

where “cloud” refers to all pixels spanned by each cloud above $(n/T_s)_{\text{thresh}} = 0.002 \text{ cm}^{-3}/\text{K}$.

In Figure 4, we compare the true and observed spin temperature for all clouds with AGD matches in absorption and emission according to Equations 5, 7, 8 and 9. The AGD and true estimates agree within the 1 σ contours of Figure 4. However, at high temperatures, where $T_{s,\text{true}} > 400 \text{ K}$, the AGD temperature overestimates the true cloud temperature.

To understand why AGD overestimates spin temperature at high temperatures, Figure 5 displays a set of example matched spectral lines with $T_{s,\text{true}} \sim 400 \text{ K}$ and $T_{s,\text{AGD}} \sim 900 \text{ K}$. We reproduce Figure 4 in the top left panel of Figure 5, and include the corresponding matched HI emission and absorption lines in the accompanying panels, highlighted with purple shading. In all highlighted cases, the emission component is slightly offset in velocity from the corresponding absorption component.

As discussed above, this offset is caused by interstellar

turbulence. When Equation 12 is applied, the resulting spin temperature will be overestimated if we do not account for this velocity offset. For example, in the examples shown in Figure 5, if we estimate the spin temperature using the peak brightness temperature and peak optical depth only, we get a value that agrees much more closely with $T_{s,\text{true}}$, as $T_{B,\text{peak}}/(1 - e^{-\tau_{\text{peak}}}) \sim 400 \text{ K}$. A more complex radiative transfer treatment such as the method of HT03 and Murray et al. (2015), accounts for this effect, which is strongest for those components with the highest turbulent velocity offset between the CNM and WNM. We find that $T_{s,\text{AGD}}$ most strongly overestimates $T_{s,\text{true}}$ when the velocity offset between absorption and emission is highest. However, most components are not affected. We will fine-tune our radiative transfer treatment in future work.

5.4.2. Column Density

The HI column density ($N(\text{HI})$) is given by,

$$N(\text{HI}) = C_0 \int T_s(v) \tau(v) dv, \quad (14)$$

where $C_0 = 1.813 \times 10^{18} \text{ cm}^{-2} \text{ K}^{-1} (\text{km s}^{-1})$. For a pair of matched AGD absorption and emission lines, we compute the column density per component ($N(\text{HI})_{\text{AGD}}$) as,

$$N(\text{HI})_{\text{AGD}} = C_0 T_{s,\text{AGD}} \int \tau_{\text{AGD}}(v) dv \quad (15)$$

where $T_{s,\text{AGD}}$ is computed using Equation 12 and $\tau_{\text{AGD}}(v)$ is the Gaussian function fitted by AGD to $\tau(v)$.

The true, simulated column density of each cloud is given by,

$$N(\text{HI})_{\text{true}} = \int_{\text{cloud}} n(s) ds \quad (16)$$

where the integration bounds of “cloud” refers to all pixels spanned by each cloud above $(n/T_s)_{\text{thresh}} = 0.002 \text{ cm}^{-3}/\text{K}$.

In Figure 6, we compare the true and observed column density for all clouds with AGD matches in absorption and emission according to Equations 5, 7, 8 and 9. As in Figure 4, the AGD and true estimates agree within the 1 σ contours. However, outside the 1 σ contours, $N(\text{HI})_{\text{AGD}}$ appears to overestimate $N(\text{HI})_{\text{true}}$, likely because any uncertainty in $T_{s,\text{AGD}}$ is propagated to $N(\text{HI})$ via Equation 15. We color the points in Figure 6 by $T_{s,\text{AGD}}$ to illustrate this. The most discrepant points correspond to the highest values of $T_{s,\text{AGD}}$, where the uncertainty in the matching process is highest (c.f., Figure 4).

In Figure 7, we investigate the scatter present in Figures 4 and 6 by plotting the ratios of the observed (“AGD”) to simulated (“true”) estimates of spin temperature and column density as a function of various LOS parameters. These include Galactic longitude (l ; a), absolute Galactic latitude ($|b|$; b), and the peak optical depth of the matched AGD line (τ_0 ; c). In each panel, the data points are colored according to $T_{s,\text{AGD}}/T_{s,\text{true}}$ (red) and $N(\text{HI})_{\text{AGD}}/N(\text{HI})_{\text{true}}$ (blue).

In Figure 7, the ratio of AGD to true spin temperature and column density falls within a factor of 2 for the majority (68%, 1 σ contours) of clouds at all longitudes (a), latitudes (b) and peak optical depths (c) probed.

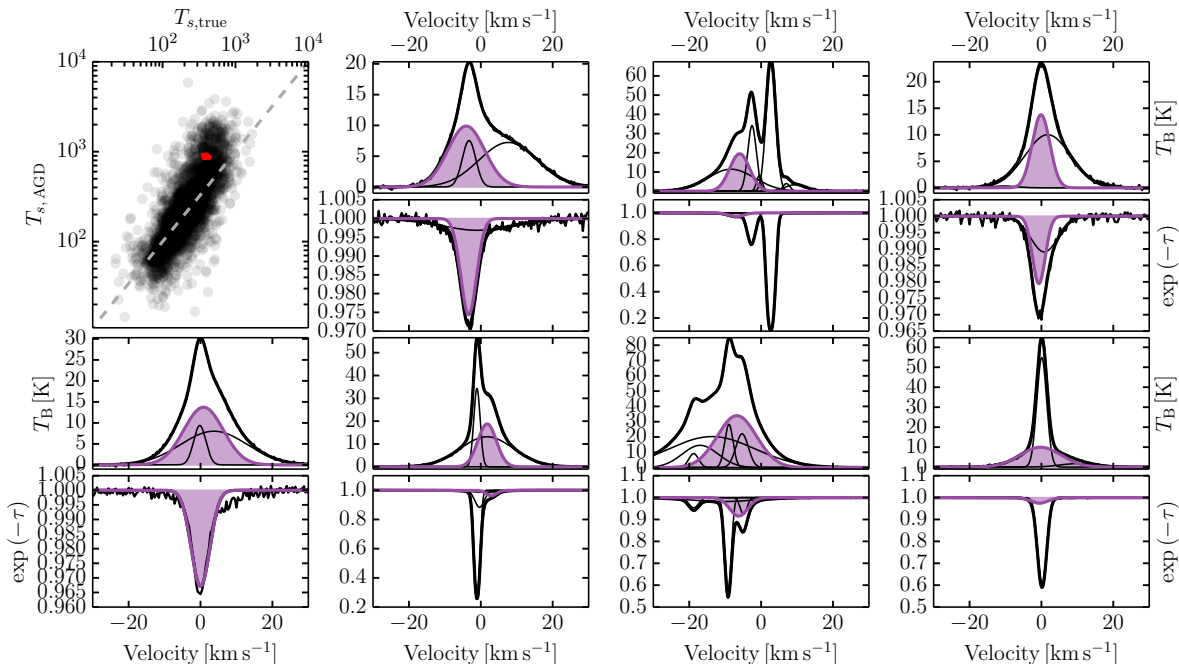


FIG. 5.— Example synthetic HI emission and absorption spectral pairs in which the AGD-derived spin temperature ($T_{s,\text{AGD}}$) overestimates the simulated spin temperature ($T_{s,\text{true}}$). The top-left panel is reproduces Figure 4, with 7 examples around $T_{s,\text{true}} = 400$ K and $T_{s,\text{AGD}} = 900$ K highlighted in red. The matched HI absorption and emission pairs corresponding to these highlighted points to are plotted in purple in the accompanying panels, along with the full AGD decomposition for each spectrum.

This indicates that the AGD method is able to recover these properties reasonably well. The scatter in the ratio of AGD to true column density is also larger than for spin temperature, due to the fact that any uncertainty in $T_{s,\text{AGD}}$ is propagated to $N(\text{HI})_{\text{AGD}}$ via Equation 15.

The scatter in AGD/True appears to be constant with longitude (l), yet increases at low latitudes (b) and low

peak optical depths ($\tau_0 < 0.1$). This is caused by the increase in LOS complexity at low latitudes, whose effect was noted in Figure 3, and the increased likelihood for a low- τ_0 component to be affected by velocity blending.

However, the agreement between AGD and true spin temperature and column density for the majority of simulated clouds is encouraging, and indicates that automatic routines for identifying and analyzing real structures from observations – essential for future large observed and simulated datasets – can be successful in recovering true properties for a large fraction of clouds.

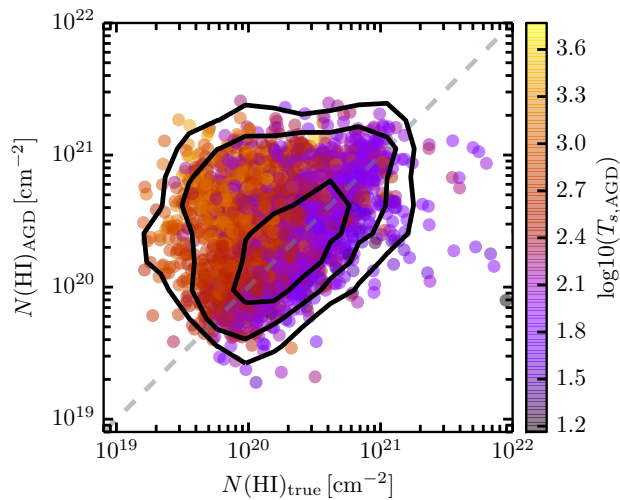


FIG. 6.— True, simulated column density ($N(\text{HI})_{\text{true}}$, Equation 16), versus observed column density ($N(\text{HI})_{\text{AGD}}$, Equation 15) for all clouds which match fitted absorption and emission lines according to Equations 5, 7, 8 and 9. Contours indicate the 1, 2 and 3σ limits.

6. COMPARING REAL AND SYNTHETIC HI OBSERVATIONS

After analyzing the biases of Gaussian analysis in recovering clouds and their properties using synthetically-observed simulations, we move on to compare observed (21-SPONGE) and simulated (KOK14) HI spectra via AGD-fitted Gaussian parameters.

With the AGD decompositions of HI emission and absorption for all 21-SPONGE and KOK14 LOS, we apply the criteria described by Equations 8 and 9 to match as many AGD lines between absorption and emission as possible. For KOK14, this does not take into account matching with clouds along the LOS as described in Section 5, in the interest of eliminating as many biases as possible in our comparison between the matching statistics of KOK14 and 21-SPONGE (which does not have cloud information).

Figure 8 displays the matches between HI absorption and HI emission for a set of 5 example observed LOS from 21-SPONGE. All components fitted by AGD to each LOS are shown in dashed black, and the components which satisfy the matching criteria described by Equations 8 and 9 are shown in colors.

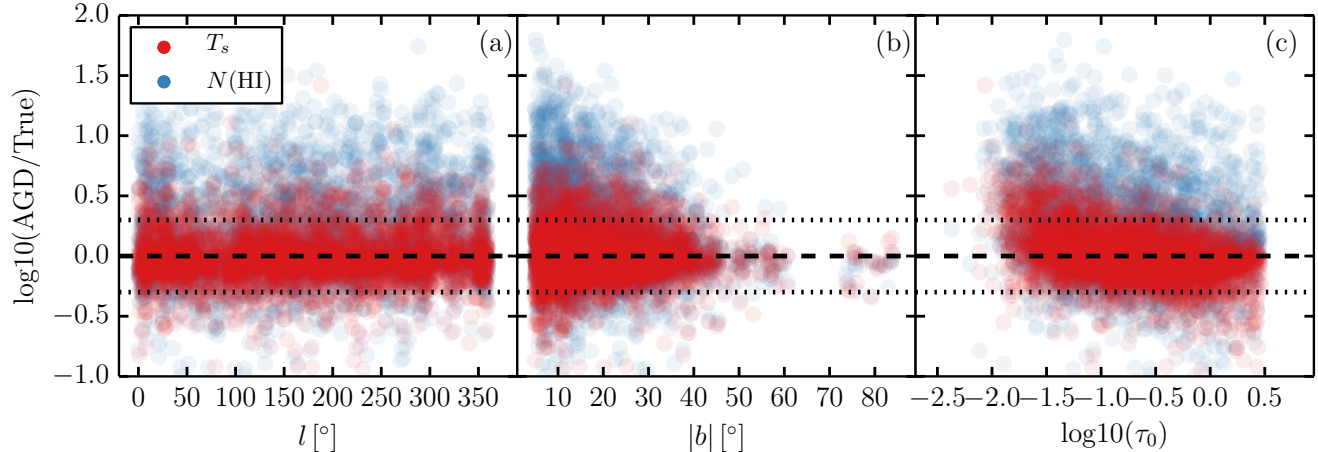


FIG. 7.— The ratio of observed (“AGD”) to simulated (“True”) properties of clouds matched with Gaussian spectral lines fitted to HI emission and absorption lines as a function of various LOS parameters. (a): Galactic longitude, l [°]; (b): absolute Galactic latitude, $|b|$ [°]; (c): peak optical depth of the matched absorption line, τ_0 ; Spin temperature, $T_{s,AGD}/T_{s,true}$ (red) and column density, $N(\text{HI})_{AGD}/N(\text{HI})_{true}$ (blue). Dotted lines indicate factors of 2.

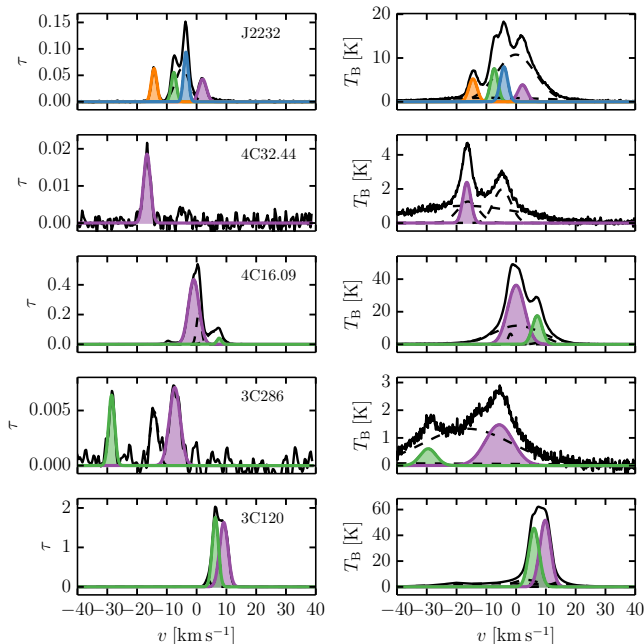


FIG. 8.— Example LOS HI absorption spectra (left) and corresponding HI emission spectra (right) from 21-SPONGE, with AGD-fitted Gaussian decompositions overlaid (dashed black). Components which match between absorption (left) and emission (right) according to Equations 8 and 9 are indicated by matching colors between the left and right columns.

6.1. Number of components along LOS

In Table 1 we list the total number of AGD components in each HI absorption and emission dataset, as well as the mean and standard deviation number of components per LOS (N_{AGD}). In addition, we list the total number of matched components between absorption and emission, and the mean and standard deviation number of matches per LOS.

Although N_{AGD} is consistent for 21-SPONGE and all KOK14 simulations within 1σ for HI absorption and

emission, the mean value is more than a factor of two greater for the observed 21-SPONGE HI absorption and emission spectra. Figure 9 displays histograms of N_{AGD} for 21-SPONGE (top left panel) and KOK14 (bottom left panel) absorption (black solid) and emission (orange dashed) components. In agreement with the statistics shown in Table 1, the maximum number of components fitted to 21-SPONGE absorption (12) is a factor of two higher than KOK14 (6)..

The larger number of components found in the 21-SPONGE spectra suggests that the path length used to produce the KOK14 synthetic spectra is shorter than what is sampled by observations. The KOK13 simulations are known to have a relatively low vertical velocity dispersion ($\sim 5 - 7 \text{ km s}^{-1}$) and no magnetic fields, and therefore the scale heights for the CNM tend to be unrealistically small. In more recent work, Kim & Ostriker (2015) showed that magnetic fields do not affect the scale heights strongly in the context of star formation self-regulation. However, their small vertical velocity dispersion reduces the number of synthetically-observed cloud components along each LOS, and future simulations (Kim et al. in preparation) will improve these conditions.

We emphasize that the results shown in Figure 9 are derived from identical implementation of AGD to real and synthetic observations, and are unaffected by biases introduced in spectral line analysis. Therefore, although the caveats described above are known from external analysis of the KOK13 simulations, Figure 9 suggests that N_{AGD} reflects simulated path lengths and the HI scale height.

To test this, in the right panels of Figure 9, we plot histograms of the number of AGD lines per unit path length $N_{AGD} \times \sin |b|$, for all HI absorption (black) and emission (orange) observations from 21-SPONGE and KOK14. When the path length is corrected for, we still find more components per LOS in 21-SPONGE than in KOK14. This indicates that additional effects are important.

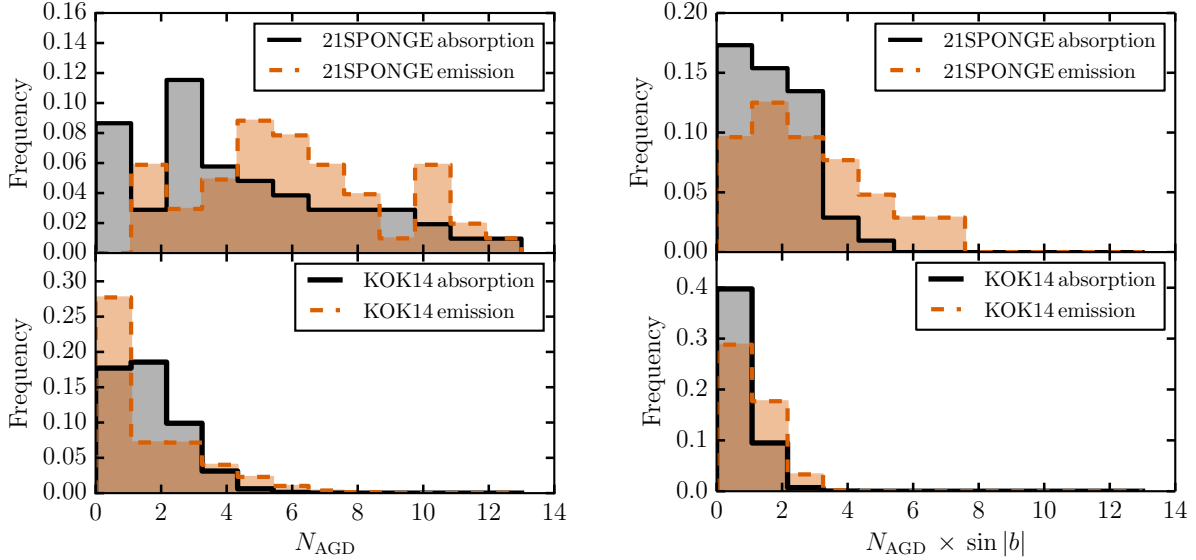


FIG. 9.— Left: Histograms displaying number of AGD lines (N_{AGD}) fit to HI absorption (black) and emission (orange) observations from 21-SPONGE (top) and synthetic observations by KOK14 (bottom). Right: Histograms displaying number of AGD lines per unit path length ($N_{\text{AGD}} \times \sin|b|$) for HI absorption (black) and emission (orange) observations from 21-SPONGE (top) and synthetic observations by KOK14 (bottom).

Furthermore, from Table 1, although the number of matches per LOS is consistent with the number of fitted lines per LOS (N_{AGD}) in KOK14, there are comparatively fewer matches per LOS than N_{AGD} in 21-SPONGE. This difference likely comes from the so-called mismatch of angular resolution, an issue that plagues all absorption observations. In 21-SPONGE, the angular resolution of the HI absorption measurements is determined by the size of the background source, not the telescope beam (and is therefore $< 1 - 40''$). However, the HI emission spectrum has an angular resolution of $3.5'$. Therefore, the HI emission spectrum may not sample the same clouds seen in absorption, especially if there is significant emission structure on angular scales below the resolution limit. This mismatch complicates the matching process and causes a larger attrition rate for observations. Simulations, on the other hand, do not suffer from this problem, as emission and absorption are derived using the same angular resolution. In the future, we plan to quantify this effect by smoothing simulated spectra.

6.2. Properties of HI absorption components

To compare 21-SPONGE and KOK14, Figure 10 displays cumulative distribution functions (CDFs) of Gaussian parameters fitted by AGD to HI absorption spectra observed by 21-SPONGE (black) and simulated by KOK14 with (blue) and without (orange) the WF effect, normalized by the total number of components (see Table 1). These parameters include amplitude (τ_0 ; left panel), FWHM (Δv_0 in km s^{-1} ; center panel) and mean velocity (v_0 in km s^{-1} ; right panel). For each dataset, we also plot the CDFs of 1000 bootstrapped samples (shown in lighter-shaded colors according to the legend) to illustrate the effect of sample size and outliers on the shape of the CDF.

6.2.1. Comparison with previous studies

We include the results of the by-hand Gaussian decomposition of the first 31/52 21-SPONGE sources (dashed purple; Murray et al. 2015, “DR1”) and the Millennium Arcibo 21cm Absorption Line Survey (dashed green; HT03) in Figure 10. With lower sensitivity in optical depth, the HT03 distribution contains fewer $\tau_0 < 10^{-2}$ components than are found in the 21-SPONGE or KOK14 AGD decompositions. However, the 21-SPONGE DR1 τ_0 distribution agrees very well with the 21-SPONGE AGD distribution, which indicates that although the AGD algorithm was trained using component parameters from HT03, it is successfully able to recover lower- τ amplitudes found in the higher-sensitivity 21-SPONGE and KOK14 spectra. This agreement was also noted in the comparison between by-hand and AGD analysis of a subset of the 21-SPONGE sample (Lindner et al. 2015). In addition, the 21-SPONGE AGD Δv_0 distribution agrees very well with DR1 and HT03, indicating that for a wide range in optical depth sensitivity, a similar range in Gaussian spectral line widths can be recovered.

6.2.2. Influence of local box simulations

From the righthand panel of Figure 10, the observed 21-SPONGE (AGD and DR1) and HT03 absolute mean velocities ($|v_0|$) agree very well. However, the KOK14 spectra are dominated by components with $v_0 < 10 \text{ km s}^{-1}$. This difference may be caused by the fact that the KOK14 spectra are constructed with a limited path length ($s < 3 \text{ kpc}$) based on their local box simulations, in which the sources of HI lines are limited by a nearby gas with small variations of galactic rotation velocity. The limited range of v_0 in KOK14 spectra causes more components to have similar central velocity.

To test the influence of the local box and lack of global rotation effects in the simulation, we consider the effect of latitude on the matching statistics. For high latitude LOS ($|b| > 50^\circ$) in KOK14, the number of absorption

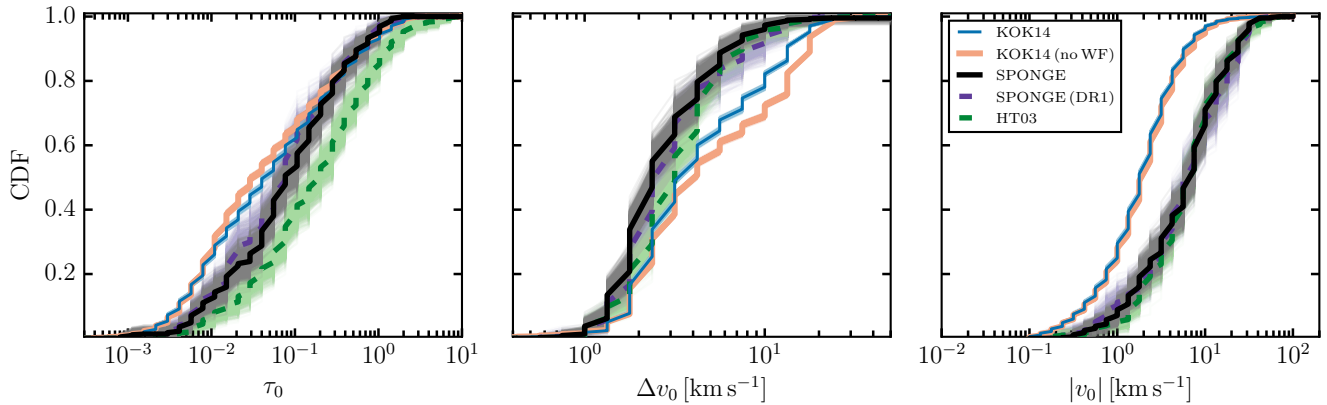


FIG. 10.— Cumulative distribution functions (CDFs) of Gaussian parameters, including optical depth amplitude (τ_0), FWHM (Δv_0) and absolute mean velocity ($|v_0|$), of the components fitted by AGD to observed (21-SPONGE), synthetic (KOK14) HI absorption spectra, including previous by-hand results from 21-SPONGE (purple, DR1; Murray et al. 2015) and HT03 (green) for comparison. For each dataset, we plot the CDFs of 1000 bootstrapped samples (shown in lighter-shaded colors according to the legend) to illustrate the effect of sample size and outliers on the CDF.

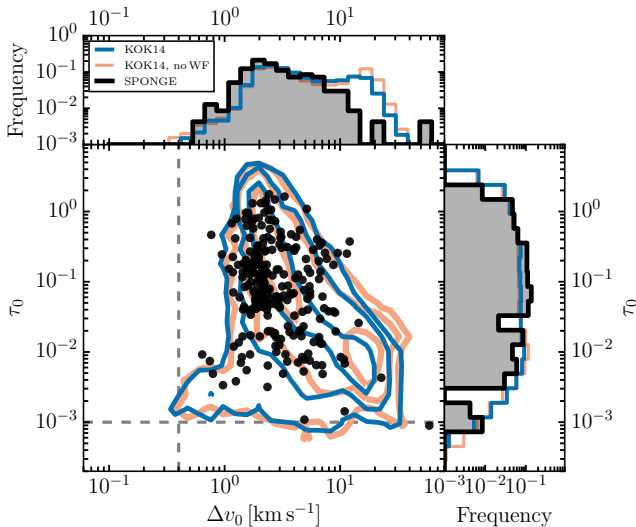


FIG. 11.— Parameters of Gaussian components (Δv_0 , τ_0) fitted by AGD to HI absorption spectra from 21-SPONGE (black) and synthetic observations of 3D hydrodynamical ISM simulations including the WF effect from KOK14 (blue). Contours indicate the 1, 2, and 3σ limits for the KOK14 distribution. Marginal histograms display results from two implementations of the WF effect from KOK14: with (blue), and without (orange), in addition to the 21-SPONGE results (black).

fits, emission fits and matches per LOS are consistent with the full sample (i.e., all latitudes). However, for 21-SPONGE, at high latitudes ($|b| > 50^\circ$) there are 1.9 ± 1.1 absorption fits per LOS, 4.4 ± 1.7 emission fits per LOS, and 0.9 ± 0.9 matches per LOS, which is more consistent with the KOK14 results in Table 1 than the full 21-SPONGE sample at all latitudes. At high latitude, the effect of rotation curve variations on spectral line properties are minimized. The consistency in matching statistics between 21-SPONGE and KOK14 at high latitudes suggests that simulated Galactic rotation dynamics play an important role in the differences between observed and simulated spectral line properties at low latitudes. Therefore, at low latitudes, the Gaussian fitting process and the match between emission and absorption

(Equations 8 and 9) in KOK14 likely suffer from more completeness issues than in observed 21-SPONGE spectra. This also suggests that our completeness statistics in Section 5.3 will be improved in future simulations, in which a larger box, and more realistic supernova feedback are implemented to push gas to higher scale heights and a wider range in velocity.

6.2.3. Minimum CNM temperature?

To highlight the comparison between 21-SPONGE and KOK14 we plot τ_0 vs. Δv_0 in Figure 11, including marginal histograms of both parameters. The median 1σ sensitivity limit in τ is indicated by the dashed horizontal line ($\sigma_\tau = 10^{-3}$), and the 21-SPONGE velocity resolution of 0.4 km s^{-1} is indicated by the dashed vertical line.

From the top panel of Figure 11, we observe a sharp cutoff in $\Delta v_0 \sim 1-2 \text{ km s}^{-1}$ in 21-SPONGE and KOK14. If we assume a limiting line width of $\sim 1 \text{ km s}^{-1}$, in the case of no turbulent broadening, the corresponding kinetic temperature is $\sim 22 \text{ K}$. This temperature is extremely low when compared to predictions (e.g., Wolfire et al. 2003), and may occur at very low metallicity when photoelectric heating by dust is diminished (Wolfire et al. 1995). HT03 also detected very cold CNM components (17% by number, and 4% by mass), and suggested that this is evidence for the absence of photoelectric heating by dust (HT03). With a larger sample and a uniform spectral decomposition by AGD, the velocity cutoff clearly stands out. We note that the components with $\Delta v_0 < 1 \text{ km s}^{-1}$ in 21-SPONGE and KOK14 are likely spurious fits, given that the accuracy of the AGD decomposition is known to be 80% in absorption (c.f., Section 4).

As shown in Figure 11, the peak optical depth spans the whole parameter space all the way to our sensitivity limit with no obvious evidence for the existence of a minimum optical depth for the CNM. In addition, only a small fraction, $< 10\%$, of components have $\tau_0 > 1$ in KOK14 and 21-SPONGE.

6.2.4. Role of the WF effect

As seen most clearly in the main panel of Figure 11, the KOK14 spectra with and without the WF effect in-

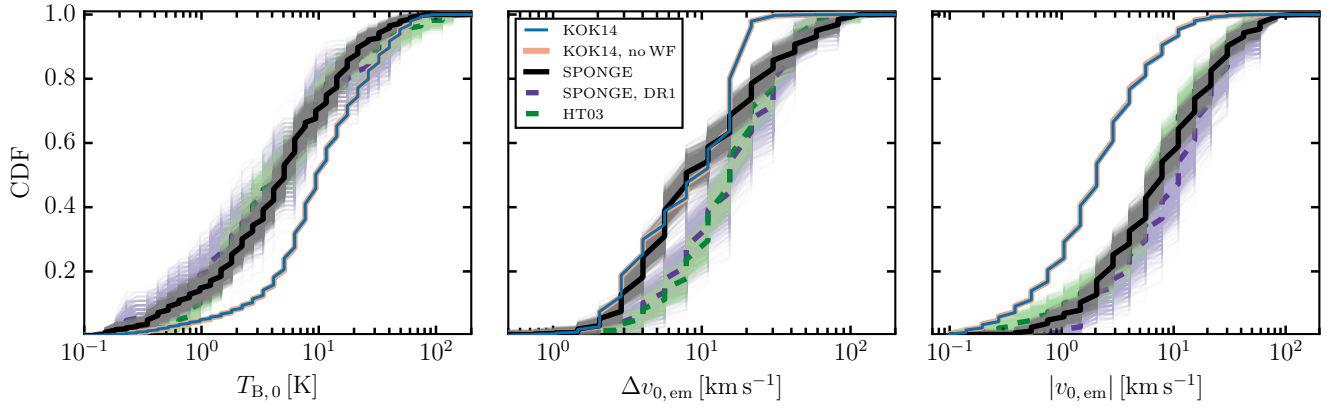


FIG. 12.— Cumulative distribution functions (CDFs) of Gaussian parameters, including brightness temperature amplitude (T_B), FWHM (Δv_0) and mean velocity (v_0), of the components fitted to observed (21-SPONGE) and synthetic (KOK14) HI emission spectra, including previous by-hand results from 21-SPONGE (purple, DR1; Murray et al. 2015) and HT03 (green) for comparison. For each dataset, we plot the CDFs of 1000 bootstrapped samples drawn from the full sample with replacement (shown in lighter-shaded colors according to the legend) to illustrate the effect of sample size and outliers on the CDF.

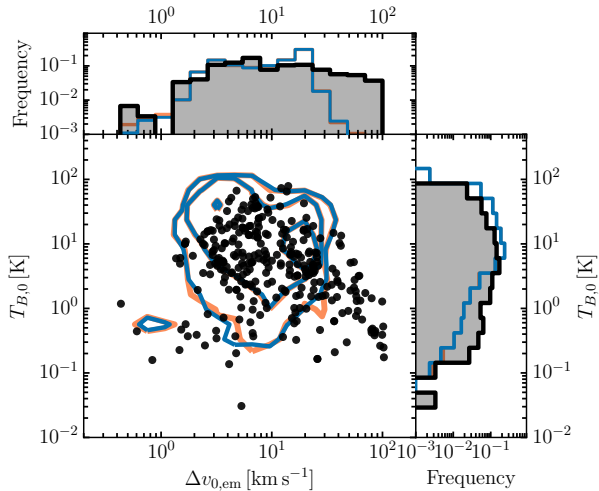


FIG. 13.— Parameters of Gaussian components (FWHM, $T_{B,0}$) fitted by AGD to HI emission spectra from 21-SPONGE (black) and KOK14 synthetic observations including the WF effect (blue) and without the WF effect (orange). Contours indicate the 1, 2, and 3σ limits for the KOK14 distribution.

clude significant populations of components with $\Delta v_0 > 10 \text{ km s}^{-1}$ and $0.001 < \tau_0 < 0.01$. Although this region is located well above the 21-SPONGE median sensitivity in optical depth, we find very few 21-SPONGE components there. In addition, in KOK14, these components are often found without narrow (CNM-like) components superimposed along the same LOS. This is a type of profile not seen in 21-SPONGE observations. There are no observational biases that would prevent us from seeing simple Gaussian line profiles with a peak optical depth of ~ 0.01 and a velocity FWHM of 10 km/sec. In addition, the lack of isolated (devoid of CNM), broad, WNM-like features in observations is supported by additional high-sensitivity HI absorption studies (e.g., HT03, Roy et al. 2013). An example isolated, broad absorption line from KOK14 is shown in the top row of Figure 2.

These broad components without sharp CNM features may be caused by the fixed value of n_α in KOK14, which causes all WNM to have the same spin temperature. In a realistic ISM, this value should vary from region to re-

gion and will broaden the distributions of τ_0 and Δv_0 . The contours in Figure 11, indicating the 1, 2, and 3σ limits, show that the inclusion of the WF effect most significantly affects the large- Δv_0 and low- τ_0 regime. However, although including the WF effect brings the synthetic τ_0 and Δv_0 distributions closer to those observed by 21-SPONGE, additional explanation is required for the remaining discrepancy and the lack of observed broad components. Future work with additional simulations is clearly needed, however it is already encouraging that HI absorption spectra are sensitive to input physics and that AGD decomposition is an effective tool for comparing observations and numerical simulations.

6.3. Properties of HI emission components

Before comparing the properties of HI emission components in the same manner as in our comparison of absorption components in Section 6.2, we emphasize again that the 21-SPONGE and KOK14 emission profiles are derived from different angular scales. The angular resolution of the KOK14 emission spectra is the same as for the absorption lines. However, the 21-SPONGE emission spectra were observed at Arecibo Observatory, with a $\sim 3.5'$ beam at 21 cm derived from off-target positions, and therefore have different angular resolution than the 21-SPONGE VLA absorption spectra. These differences are likely to affect the properties of the HI emission components. In addition, the physical resolution of the KOK14 simulation is 2 pc. For predominantly local gas at a distance of 100 to 500 pc, this corresponds to an angular resolution of $60' - 15'$. Therefore, the angular resolution of synthetic emission spectra is actually worse than 21-SPONGE observations for local gas. The situation reverses only at a distance $> 2 \text{ kpc}$. We stress that absorption lines do not have the resolution problem and this also the reason why they are more suitable for comparison with simulations.

In addition, the 21-SPONGE HI emission observations have not been corrected for stray radiation. As discussed in Murray et al. (2015), due to the complex beam pattern of the Arecibo telescope, HI emission can be contaminated at some level by radiation from higher-order side lobes. This stray radiation appears in emission spectra as broad, wing-like features at high velocities. In Murray

et al. (2015), we compared 21-SPONGE emission spectra with the GALFA-HI (Peek et al. 2011) and LAB surveys (Kalberla et al. 2005) and concluded that difference are generally within 3σ errors. Modeling stray radiation especially for Arecibo is a complex problem which will require additional attention in the future.

Figure 12 displays CDFs of Gaussian parameters from the fits to HI emission spectra observed by 21-SPONGE (black), simulated by KOK14 with the WF effect (blue) and without the WF effect (orange), in addition to the results of HT03 (green) and 21-SPONGE DR1 (purple). These parameters include amplitude in brightness temperature ($T_{B,0}$ in K; left), FWHM ($\Delta v_{0,\text{em}}$ in km s^{-1} ; center) and mean velocity ($v_{0,\text{em}}$ in km s^{-1} ; right). To illustrate the comparison between 21-SPONGE and KOK14 further, we display $T_{B,0}$ vs. $\Delta v_{0,\text{em}}$ for 21-SPONGE and KOK14 in Figure 13, with marginal histograms for both parameters. We note that the WF effect does not make a difference to components fitted to HI emission spectra (i.e., orange and blue lines are indistinguishable in Figure 12). This indicates that future testing of the implementation of the WF effect should use absorption, rather than emission spectra.

6.3.1. Boundaries in brightness temperature

In the left panel of Figure 12 (as well as Figure 13), the amplitudes fitted by AGD to 21-SPONGE agree well with 21-SPONGE DR1 and HT03. All three datasets were obtained at the Arecibo Observatory, and therefore they have the same angular resolution. However, all three observed distributions are shifted to slightly lower amplitude in brightness temperature ($T_{B,0} < 10\text{ K}$) relative to KOK14 in Figure 12. The difference in angular resolution between KOK14 and 21-SPONGE makes this discrepancy worse than it appears. As explained earlier, the simulated HI emission spectra generally have lower angular resolution than the observed HI emission spectra (at least by a factor of ~ 4). This means that KOK14 $T_{B,0}$ should be lower than the observed values, given that synthetic observations are averaging over larger solid angles. However, this is not the case.

Furthermore, the relative paucity of components with low $T_{B,0}$ in KOK14 may be caused by the lack of chemistry and HI-to-H₂ transition. These effects would lower $T_{B,0}$ on the high-end of its distribution. Our observations may even suggest an upper-limit on $T_{B,0}$ of $\sim 60 - 70\text{ K}$. In addition, on the low-end of the distribution the absence of a large filling-factor ($\sim 50\%$) hot ($T \sim 10^5 - 10^6\text{ K}$) medium in the simulations produces too much neutral gas per LOS, and therefore too few LOS with $T_{B,0} < \text{a few K}$. This same mechanism may explain the prevalence of low- τ_0 components in KOK14. A hot medium component would reduce the number of LOS with detectable, low- τ_0 components.

6.3.2. Broad emission components

In the middle panel of Figure 12, the 21-SPONGE and KOK14 $\Delta v_{0,\text{em}}$ distributions agree very well below $\Delta v_{0,\text{em}} \sim 10\text{ km s}^{-1}$. However, the 21-SPONGE AGD, DR1 and HT03 distributions extend to higher values of $\Delta v_{0,\text{em}}$ than KOK14. This is especially noticeable in Figure 13 where 21-SPONGE components with large $\Delta v_{0,\text{em}}$ and small $T_{B,0}$ form a prominent tail of the distribution. As mentioned earlier, stray radiation would

produce weak and broad spectral components. To test how many 21-SPONGE components could be affected by stray radiation, we extracted HI emission spectra from the stray-radiation-corrected LAB survey (Kalberla et al. 2005) at the positions of our sources. We implemented AGD in same manner to decompose LAB HI emission spectra into Gaussian components. Consequently, LAB data contain many components with $\Delta v_{0,\text{em}} \sim 10 - 80\text{ km s}^{-1}$ (c.f., Appendix). However, components with $\Delta v_{0,\text{em}} \gtrsim 70 - 80\text{ km s}^{-1}$ are not seen LAB data, and therefore those components in 21-SPONGE are likely caused by stray radiation. There are 9 such components and they are all located in the large $\Delta v_{0,\text{em}}$ and small $T_{B,0}$ tail. Peek et al. (2011), did a similar comparison between LAB and Arecibo data and concluded that stray radiation is unlikely to exceed 500 mK. This agrees with our conclusion that only the broadest 21-SPONGE components with $T_{B,0} < 0.5\text{ K}$ are likely caused by stray radiation.

This leaves a population of broad ($\Delta v_{0,\text{em}} \gtrsim 20 - 70\text{ km s}^{-1}$), shallow ($T_{B,0} < 10\text{ K}$) components that are prominent in 21-SPONGE but absent in KOK14. Possibly a higher velocity dispersion and the inclusion of Galactic fountain in the simulation may be able to reproduce such broad lines. Alternatively, this could signify the presence of the WNM at temperature $> 4000\text{ K}$. For example, Murray et al. (2014) detected a residual absorption component with a width of 50 km/s and $T_s \sim 7000\text{ K}$ by stacking the first third of the 21-SPONGE data. Further work is clearly needed to understand the origin of such broad emission components, as well as to remove stray radiation from Arecibo spectra.

Finally, in the right panel of Figure 12, all observed HI emission spectra have absolute mean velocities up to $\sim 50\text{ km s}^{-1}$, whereas the KOK14 mean velocities appear limited to $v_{0,\text{em}} < 10\text{ km s}^{-1}$ (c.f., right panel Figure 10). In addition to the nature of the local box reducing $|v_{0,\text{em}}|$, the KOK13 simulations did not include a Galactic fountain of WNM with velocities up to tens of km s^{-1} . The inclusion of this important mechanism may produce relatively more structures with larger $|v_{0,\text{em}}|$ and $\Delta v_{0,\text{em}}$ and improve similarities between the 21-SPONGE and KOK14 results.

6.4. Observed vs. Simulated Spin Temperature

We now compare distribution functions of 21-SPONGE and KOK14 AGD-derived spin temperature, $T_{s,\text{AGD}}$. As we have shown in Section 5.4.1, for the majority of cases our spin temperature derived using AGD and a simple radiative transfer approach is in agreement with the true simulated temperature, $T_{s,\text{true}}$. We also discussed how at $> 400\text{ K}$, $T_{s,\text{AGD}}$ over-estimates $T_{s,\text{true}}$. However, this bias will affect both observations and simulations in the same way, as we apply the same AGD fit and radiative transfer method to KOK14 and 21-SPONGE. In addition, our main focus in this paper is on the shape of distribution functions, not the exact fractions. In future work, we will focus on the fractions of HI in CNM, WNM and unstable phases using updated simulations.

Figure 14 displays histograms and CDFs of $T_{s,\text{AGD}}$ (Equation 12) for 21-SPONGE (black) and KOK14 with (blue) and without (orange) the WF effect. The observed and simulated $T_{s,\text{AGD}}$ distributions follow each

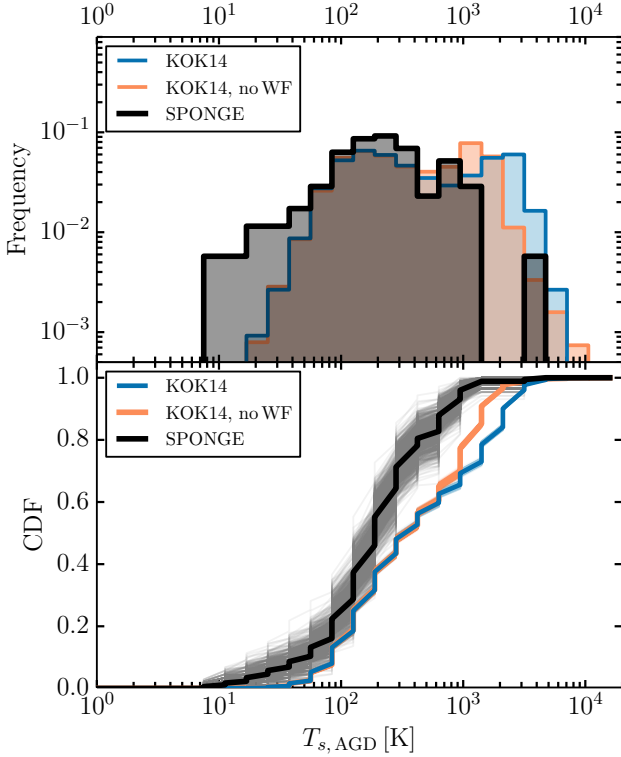


FIG. 14.— Top: histograms of $T_{s,AGD}$ (Equation 12) for all components which “match” between HI emission and absorption (Equations 8 and 9) following the AGD analysis of 52 21-SPONGE HI spectral pairs (thick, solid black) and 9355 KOK14 HI spectral pairs with the WF effect (thin, solid blue) and without the WF effect (thin, solid orange). Bottom: CDFs of the same results, with 1000 bootstrapped samples drawn from the full sample with replacement (shown in lighter-shaded colors according to the legend) to illustrate the effect of sample size and outliers on the CDF.

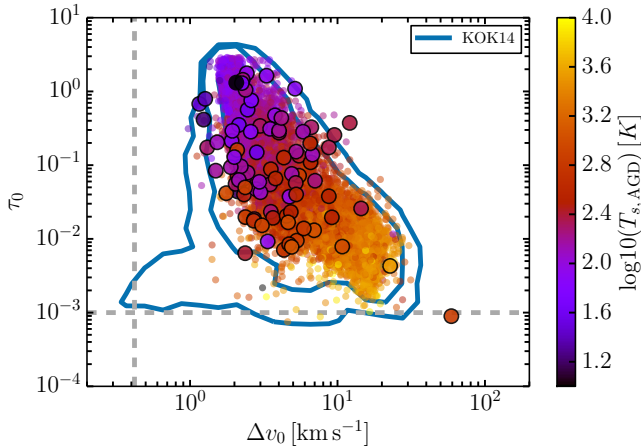


FIG. 15.— AGD absorption properties (τ_0 , Δv_0) for all components fitted to KOK14 (blue contours), and all components which match between absorption and emission according to Equations 8 and 9 for KOK14 (small circles) and 21-SPONGE (large circles with black outlines), colored by the AGD spin temperature ($T_{s,AGD}$).

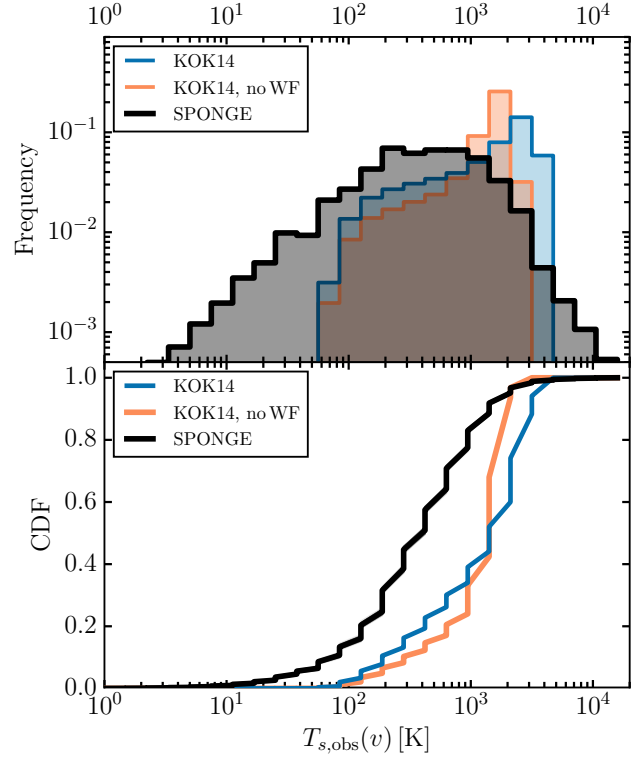


FIG. 16.— Top: histograms of per-channel spin temperature ($T_s(v)$) for all 52 21-SPONGE HI spectral pairs (thick, solid black) and 9355 KOK14 HI spectral pairs with the WF effect (thin, solid blue) and without the WF effect (thin, solid orange). Bottom: CDFs of the same results.

other well and agree within uncertainties until $T_{s,AGD} \sim 400 - 500$ K, when they start to diverge. Observations show more cold HI, which is expected due to lack of H_2 formation in the KOK13 simulations. The KOK14 spectra show more HI with $T_{s,AGD} = 300 - 3000$ K than 21-SPONGE. As shown in Figure 15, and AGD components with $T_{s,AGD} \sim 300 - 3000$ K in the simulation have lowest optical depth and the largest FWHM. These are exactly the components discussed in Section 6.2 to have simple, broad profiles without overlapping CNM components – a type of spectral profile which is not found often in 21-SPONGE.

Are the differences in $T_{s,AGD}$ between KOK14 and 21-SPONGE caused by observational sensitivity? 21-SPONGE has excellent sensitivity (RMS optical depth noise $\sigma_\tau < 10^{-3}$ per channel) and it was designed with goal of detecting warm HI in absorption. To estimate the temperatures we are sensitive to in 21-SPONGE observations, we assume a WNM column density of a few $\times 10^{20}$ (e.g., Stanimirović et al. 2014, , KOK14), a FWHM of $10 - 20$ km s $^{-1}$ and a conservative RMS sensitivity in optical depth of $10^{-2} - 3 \times 10^{-3}$ (per 0.4 km/s velocity channels), which results in $T_s \sim 1000 - 6000$ K. This is the range of what is expected by KOK14 and also Liszt (2001). Therefore, 21-SPONGE has the observational sensitivity to detect spectral components with $T_s > 1000$ K. Strong, CNM-like absorption lines are easy to detect in HI spectra, and whether or not our analysis

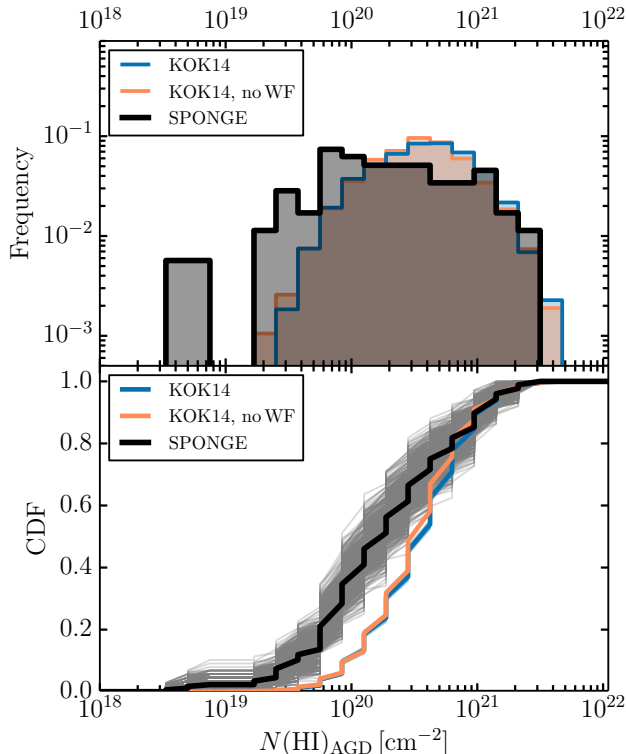


FIG. 17.— Top: histograms of $N(\text{HI})_{\text{AGD}}$ (Equation 15) for all components which “match” between HI emission and absorption (Equations 8 and 9) following the AGD analysis of 52 21-SPONGE HI spectral pairs (thick, solid black) and 9355 KOK14 HI spectral pairs with the WF effect (thin, solid blue) and without the WF effect (thin, solid orange). Bottom: CDFs of the same results, with 1000 bootstrapped samples drawn from the full sample with replacement (shown in lighter-shaded colors according to the legend) to illustrate the effect of sample size and outliers on the CDF.

methods bias our ability to detect broad and weak spectral lines from the WNM has long been an open question. We have demonstrated in Section 5.4.1 that AGD and our radiative transfer implementation are not biased against WNM. Therefore, we can infer that the lack of observed components with $T_s > 1000$ K is a robust result, and is not affected by sensitivity or analysis methods. In addition, we emphasize again that the $T_s > 1000$ K components in simulations have isolated, simple spectral profiles that we do not find in observations.

So, what causes the discrepancy shown in Figure 14? With initial data from the 21-SPONGE survey, Murray et al. (2014) investigated methods for improving our sensitivity to broad, shallow WNM-like absorption lines even further. We stacked residual HI absorption lines of a subset of sources following by-hand Gaussian decomposition and found a residual HI absorption signal at 5σ significance with an inferred excitation temperature of $T_s = 7200_{-1200}^{+1800}$ K, with a FWHM of 50 km s^{-1} , and an HI column density of $2 \times 10^{20} \text{ cm}^{-2}$ (Murray et al. 2014). This temperature is higher than analytical predictions for collisional excitation of HI, and indicated that additional HI excitation mechanisms (e.g., the WF effect) may be more important for coupling the hyperfine spin states of HI to the local thermodynamic temperature than previ-

ously thought.

If the spin temperature of the WNM is actually $T_s \sim 7000$ K (Murray et al. 2014), rather than $2000 < T_s < 4000$ K as inferred currently from analytical models of collisional excitation (e.g., Liszt 2001), then it is possible that individual 21-SPONGE spectra may still lack sensitivity for detecting the WNM. Even more sensitive observations, as well as further stacking analysis will be essential from an observational standpoint. This result shows that understanding the implementation of the WF effect in numerical simulations, and in particular the highly uncertain n_α , its spatial variations across the Milky Way, as well as the effect of turbulence, is essential to reconcile HI observations and theory.

6.4.1. Per-channel T_s

Instead of using Gaussian-based temperature estimates, KOK14 considered per-channel spin temperature in their analysis of synthetically-observed HI properties. They found that this quantity agrees well with the true per-channel temperature extremely well (within a factor of 1.5) for all channels with $\tau \lesssim 1$ (KOK14). Several observational studies have also used per-channel temperature estimates to analyze HI phases (e.g., Roy et al. 2013). To compare with their results, we derive per-channel spin temperature, $T_{s,\text{obs}}(v)$, by applying an equation similar to Equation 11 to the full $\tau(v)$ and $T_B(v)$ spectra from 21-SPONGE and KOK14, where,

$$T_{s,\text{obs}}(v) = \frac{T_B(v)}{1 - e^{-\tau(v)}}, \quad (17)$$

For each LOS, we compute $T_{s,\text{obs}}(v)$ for only those channels with optical depths greater than 3×10^{-3} , to conservatively exclude all channels with low S/N.

In Figure 16, we display histograms and CDFs of $T_{s,\text{obs}}(v)$ for 21-SPONGE (black) and KOK14 with (blue) and without (orange) the WF effect. There is a similar discrepancy between observations and simulations in Figure 16 as seen in Figure 14. The KOK14 distributions are shifted to higher temperatures, while 21-SPONGE spectra contain more channels with low temperature (< 200 K). In addition, the 21-SPONGE CDF has a more gradual rise, while simulated data show an abrupt jump near $T_{s,\text{obs}}(v) \sim 1000$ K suggesting that most simulated LOSs are dominated by higher $T_{s,\text{obs}}(v)$ derived from spectral channels without detectable absorption. It is important to keep in mind, however, that observed and simulated spectra probe different LOS lengths, as discussed in Section 6.2, which could affect the shape of per-channel CDFs.

6.5. Observed vs. Simulated Column Density

As a further benefit of AGD analysis, by resolving the properties of individual spectral components along each LOS, we can analyze the column densities of individual clouds in contrast with the total LOS column density. In Figure 17, we display histograms and CDFs of $N(\text{HI})_{\text{AGD}}$ for individual matched spectral components from the KOK14 (blue) and 21-SPONGE (thick black) HI emission and absorption spectral pairs. The column density distributions shown in Figure 17 agree well at high- $N(\text{HI})$ ($> 10^{20} \text{ cm}^{-2}$), although the 21-SPONGE distribution extends further below $N(\text{HI}) = 10^{19} \text{ cm}^{-2}$.

The absence of low-column lines in the KOK14 spectra may be caused by insufficient angular resolution for detecting small CNM clouds, or, as has been mentioned throughout, the absence of a hot medium in the KOK13 simulations which would serve to reduce the observed column densities of the matched lines. The discrepancy around 10^{20} cm^{-2} is likely caused by the discrepancy in $T_{s,\text{AGD}}$ discussed above in Section 6.4. It is interesting to note that the application of the WF effect does not significantly affect the $N(\text{HI})_{\text{AGD}}$ distribution. The WF effect influences the optical depth and spin temperature in opposite ways, i.e., increases T_s and decreases τ . These quantities are the main ingredients of $N(\text{HI})_{\text{AGD}}$ (c.f., Equation 15), and therefore the two results of the WF effect may cancel each other out when computing component-based column density. We conclude that the complexity of factors incorporated into the HI column density make it a less useful tool for isolating the importance of the WF effect.

7. SUMMARY AND CONCLUSIONS

Comparisons between observations and simulations are crucial for understanding the physics behind the observed properties of the ISM. Armed with synthetic HI observations of 3D hydrodynamical simulations from KOK14 and high-sensitivity HI observations from 21-SPONGE, we address two main questions: (1) how well do HI spectral lines and our analysis methods recover true properties of interstellar clouds? (2) how do simulated HI spectra compare with real observations? To analyze 9355 synthetic and 52 real observations in an unbiased and uniform way, we apply the Autonomous Gaussian Decomposition (AGD) algorithm (Lindner et al. 2015) identically to both datasets. With these fits in hand, we compare simulated properties of clouds along each line of sight with observed properties of the Gaussian components.

We summarize the main results:

1. For clouds defined by peaks in n/T_s along random LOS in the KOK13 simulations, Gaussian fits by AGD to synthetic HI absorption lines are able to recover clouds successfully (Figure 3). The recovery completeness (Equation 10) is 100% for high-latitude LOS ($|b| > 50^\circ$), 76% for mid-latitude LOS ($20 < |b| < 50^\circ$) and 54% for low-latitude LOS ($0 < |b| < 20^\circ$). The completeness declines with decreasing latitude because the LOS complexity is highest at the lowest latitudes. When these clouds are matched to spectral line components in both HI absorption and emission, the completeness is 89%, 41% and 29% for high, mid and low latitudes respectively. The decline in cloud recovery completeness when matches between clouds and both HI absorption and emission are required reflects the difficulty in associating unambiguous spectral features in the presence of line blending and turbulence.
2. We use AGD fits to compute observational estimates of spin temperature ($T_{s,\text{AGD}}$) and column density ($N(\text{HI})_{\text{AGD}}$) for matched pairs of HI absorption and emission lines. We compare these estimates with the true, simulated spin temperatures ($T_{s,\text{true}}$) and column densities ($N(\text{HI})_{\text{true}}$) of

corresponding clouds. The observed and true spin temperatures agree within a factor of 2 for the majority of clouds (68%; Figure 4). At high temperatures, $T_{s,\text{AGD}}$ overestimates the $T_{s,\text{true}}$ due to velocity offsets between HI absorption and emission lines caused by turbulent cloud motions (Figure 5).

The observed and true estimates of HI column density also agree well for the majority of clouds. However, the scatter is slightly larger than in the case of spin temperature, because $N(\text{HI})_{\text{AGD}}$ incorporates all uncertainty in $T_{s,\text{AGD}}$ (Figure 6). Furthermore, the agreement between observed and true properties declines at low Galactic latitude and for low- τ components, where LOS-blending components hinder clear associations between emission and absorption spectral lines (Figure 7).

Overall, the agreement between temperature and column densities inferred from synthetic observations and true simulated conditions is encouraging. Future comparisons with next-generation simulations will allow us to construct “correction functions” for observed spin temperature and column density distributions.

3. We find more fitted absorption and emission lines per LOS (N_{AGD}) in the 21-SPONGE observations than the KOK14 synthetic observations (Table 1). This difference reflects the fact that the simulated scale heights of the CNM and WNM in the KOK13 simulations are too low, due to small velocity dispersions ($\sim 5 - 7 \text{ km s}^{-1}$), and the omission of magnetic fields (although the inclusion of magnetic fields does not strongly influence the CNM and WNM scale heights as shown by Kim & Ostriker 2015). These results are derived from identical implementation of AGD to 21-SPONGE and KOK14, and are unaffected by biases introduced by AGD analysis. After correcting for path length, we still find more components per LOS in 21-SPONGE than KOK14, which reflects the limitations of local box simulations in producing realistic synthetic spectral lines.

In addition, there are comparatively fewer matches per LOS in 21-SPONGE than KOK14. The so-called mismatch in angular resolution between 21-SPONGE HI emission ($\sim 3.5'$) and absorption ($1 - 40''$) complicates the matching process described by Equations 8 and 9. In the future, we plan to quantify this effect and correct the observational results by smoothing simulated spectra.

4. Using AGD, we objectively compare the properties of spectral lines fitted by AGD to HI absorption from 21-SPONGE and KOK14. The 21-SPONGE spectra have a wider range in mean velocity (right panel, Figure 10), due to the absence of a global rotation curve model in the simulations. Furthermore, at high Galactic latitudes where the influence of the global effect is weakest, N_{AGD} and matching statistics agree between 21-SPONGE and KOK14. This indicates that that simulated Galactic rotation dynamics play an important role in observed HI properties, and improved implementations of

- global effects will improve the completeness statistics of HI cloud recovery, and improve the completeness characterization discussed in Summary points 1 and 2.
5. We find that KOK14 spectra include more low- τ and high- Δv absorption lines than are seen in 21-SPONGE (Figures 10 and 11), despite being well above the 21-SPONGE sensitivity and resolution limits. These broad spectral lines are often found without narrower, blended lines, which is a profile not seen in observations by 21-SPONGE or previous HI absorption line surveys (e.g., HT03, Roy et al. 2013). These are likely motivated by the absence of a hot, large filling-factor gas phase in the KOK13 simulations (which would increase the number of LOS without detectably-absorbing neutral gas), or the implementation of a constant WF effect. In particular, we find that excluding the WF effect enhances the population of these discrepant HI absorption components, and suggests that the WF effect is important for realistic spectral line properties. These features are not obvious in comparisons of integrated or per-channel properties, and reflect the utility of studying velocity-resolved spectral components. The implementation of the WF effect in the KOK14 synthetic spectral lines is simple and relies on a fixed value of the Ly α photon number density, n_α , which is uncertain and difficult to constrain observationally or numerically.
 6. We observe a limit to HI absorption line width of $\Delta v_0 \gtrsim 1 - 2 \text{ km s}^{-1}$. One explanation is that, in the absence of turbulent line broadening, this corresponds to a minimum CNM temperature of $\sim 20 \text{ K}$, which may be explained by the absence of photoelectric heating by dust (e.g., HT03).
 7. We find that HI absorption spectra are more useful probes of ISM physics in comparison with simula-

tions than HI emission spectra. Properties of components fitted to HI emission profiles are affected by angular resolution mismatch and stray radiation, and are not sensitive to the implementation of the WF effect.

8. The AGD-derived spin temperature from KOK14 is dominated by high-temperature gas ($1000 < T_{s,AGD} < 4000 \text{ K}$) relative to 21-SPONGE. The AGD method is not biased against high temperatures, and the 21-SPONGE observations have sufficient sensitivity for detecting gas at similar values. In KOK14, the highest-temperature components have large line widths and low optical depths, which is a type of profile not seen in 21-SPONGE (Figure 15). We conclude that the lack of observed components with $T_s > 1000 \text{ K}$ is a robust result, and is not affected by sensitivity or the analysis method. We suggest that this gas may have even higher temperatures ($T_s \sim 7000 \text{ K}$) than what 21-SPONGE is sensitive to and than what the KOK14 implementation of the WF effect allows (i.e., $1000 < T_s < 4000 \text{ K}$). Again, future work is required to understand the importance of the WF effect in more detail.

Overall, we are encouraged that the AGD analysis and radiative transfer method presented here is a useful tool for diagnosing important physical conditions within ISM simulations. In the future, we will apply the strategies described here to updated simulations in order to derive correction functions for observational biases in real HI data. Upcoming large HI absorption surveys such as GASKAP at the Australian Square Kilometer Array Pathfinder (ASKAP) telescope (Dickey et al. 2013) will contribute many more sources and improve the observational statistics. The objective and efficient nature of the AGD analysis strategy presented here is well-suited for future large observed and simulated datasets, and will be important for understanding the balance of CNM and WNM in the local and extragalactic ISM.

REFERENCES

- Acreman, D. M., Dobbs, C. L., Brunt, C. M., & Douglas, K. A. 2012, *MNRAS*, 422, 241
- Baumont, C. N., Offner, S. S. R., Shetty, R., Glover, S. C. O., & Goodman, A. A. 2013, *ApJ*, 777, 173
- Begum, A., Stanimirović, S., Goss, W. M., et al. 2010, *ApJ*, 725, 1779
- Carilli, C. L., Dwarakanath, K. S., & Goss, W. M. 1998, *ApJ*, 502, L79
- Chengalur, J. N., Kanekar, N., & Roy, N. 2013, *MNRAS*, 432, 3074
- Crovisier, J., Kazes, I., & Aubry, D. 1978, *A&AS*, 32, 205
- Dickey, J. M., & Lockman, F. J. 1990, *ARA&A*, 28, 215
- Dickey, J. M., McClure-Griffiths, N. M., Gaensler, B. M., & Green, A. J. 2003, *ApJ*, 585, 801
- Dickey, J. M., McClure-Griffiths, N., Gibson, S. J., et al. 2013, *PASA*, 30, e003
- Douglas, K. A., Acreman, D. M., Dobbs, C. L., & Brunt, C. M. 2010, *MNRAS*, 407, 405
- Draine, B. T. 2011, *Physics of the Interstellar and Intergalactic Medium*
- Duarte-Cabral, A., Acreman, D. M., Dobbs, C. L., et al. 2015, *MNRAS*, 447, 2144
- Duarte-Cabral, A., & Dobbs, C. L. 2016, *MNRAS*, 458, 3667
- Dwarakanath, K. S., Carilli, C. L., & Goss, W. M. 2002, *ApJ*, 567, 940
- Falgarone, E., Lis, D. C., Phillips, T. G., et al. 1994, *ApJ*, 436, 728
- Field, G. B. 1959, *ApJ*, 129, 536
- Field, G. B., Goldsmith, D. W., & Habing, H. J. 1969, *ApJ*, 155, L149
- Hartmann, D., & Burton, W. B. 1997, *Atlas of Galactic Neutral Hydrogen*, 243
- Heiles, C., & Troland, T. H. 2003a, *ApJS*, 145, 329
- . 2003b, *ApJ*, 586, 1067
- Hennebelle, P., Audit, E., & Miville-Deschênes, M.-A. 2007, *A&A*, 465, 445
- Kalberla, P. M. W., Burton, W. B., Hartmann, D., et al. 2005, *A&A*, 440, 775
- Kim, C.-G., & Ostriker, E. C. 2015, *ApJ*, 815, 67
- Kim, C.-G., Ostriker, E. C., & Kim, W.-T. 2013, *ApJ*, 776, 1
- . 2014, *ApJ*, 786, 64
- Lazareff, B. 1975, *A&A*, 42, 25
- Lindner, R. R., Vera-Ciro, C., Murray, C. E., et al. 2015, *AJ*, 149, 138
- Liszt, H. 2001, *A&A*, 371, 698
- McClure-Griffiths, N. M., Pisano, D. J., Calabretta, M. R., et al. 2009, *ApJS*, 181, 398
- McClure-Griffiths, N. M., Stanimirovic, S., Murray, C., et al. 2015, *Advancing Astrophysics with the Square Kilometre Array (AASKA14)*, 130
- McKee, C. F., & Ostriker, J. P. 1977, *ApJ*, 218, 148

Mebold, U., Winnberg, A., Kalberla, P. M. W., & Goss, W. M. 1982, *A&A*, 115, 223
Mohan, R., Dwarkanath, K. S., & Srinivasan, G. 2004, *Journal of Astrophysics and Astronomy*, 25, 185
Murray, C. E., Lindner, R. R., Stanimirović, S., et al. 2014, *ApJ*, 781, L41
Murray, C. E., Stanimirović, S., Goss, W. M., et al. 2015, *ApJ*, 804, 89
Peek, J. E. G., Heiles, C., Douglas, K. A., et al. 2011, *ApJS*, 194, 20
Pettitt, A. R., Dobbs, C. L., Acreman, D. M., & Price, D. J. 2014, *MNRAS*, 444, 919
Roy, N., Kanekar, N., & Chengalur, J. N. 2013, *MNRAS*, 436, 2366

Saury, E., Miville-Deschênes, M.-A., Hennebelle, P., Audit, E., & Schmidt, W. 2014, *A&A*, 567, A16
Shetty, R., Glover, S. C., Dullemond, C. P., & Klessen, R. S. 2011, *MNRAS*, 412, 1686
Smith, R. J., Glover, S. C. O., Clark, P. C., Klessen, R. S., & Springel, V. 2014, *MNRAS*, 441, 1628
Stanimirović, S., & Heiles, C. 2005, *ApJ*, 631, 371
Stanimirović, S., Murray, C. E., Lee, M.-Y., Heiles, C., & Miller, J. 2014, *ApJ*, 793, 132
Wolfire, M. G., Hollenbach, D., McKee, C. F., Tielens, A. G. G. M., & Bakes, E. L. O. 1995, *ApJ*, 443, 152
Wolfire, M. G., McKee, C. F., Hollenbach, D., & Tielens, A. G. G. M. 2003, *ApJ*, 587, 278
Wouthuysen, S. A. 1952, *AJ*, 57, 31

APPENDIX

To test for the effect of stray radiation on HI emission spectra, we analyze data from the LAB survey (Kalberla et al. 2005). The LAB spectra were measured with a $\sim 35'$ beam, whose shape was carefully modeled in order to remove contamination from stray radiation. We apply the AGD algorithm in the same manner as described in Section 6.3 to LAB spectra in the direction of the 52 21-SPONGE sources. In Figure 18, we reproduce Figure 13 including the LAB decomposition in red.

From Figure 18, the LAB $\Delta v_{0,\text{em}}$ distribution is shifted to larger values relative to KOK14 and 21-SPONGE. As a result of the much larger angular resolution of the LAB survey, the AGD decomposition of LAB data in Figure 18 feature fewer narrow velocity components ($\Delta v_{0,\text{em}} < 2 \text{ km s}^{-1}$), likely because the HI emission is smoothed over larger angular scales than in the 21-SPONGE spectra (from Arecibo Observatory, with $\sim 3.5'$ angular resolution).

Furthermore, the LAB decomposition contains large-linewidth ($\Delta v_{0,\text{em}} > 30 \text{ km s}^{-1}$), low-brightness temperature ($T_{B,0} < 1 \text{ K}$) components similar to 21-SPONGE. However, there is a population of 21-SPONGE components with $\Delta v_{0,\text{em}} \sim 50 - 100 \text{ km s}^{-1}$ outside the LAB distribution. Given that stray radiation has been removed from the LAB spectra, this type of spectral feature may be indicative of stray radiation.

In a future paper, we will compare the KOK14 synthetic HI emission spectra and data from the LAB and GALFA-HI surveys objectively using AGD in order to statistically quantify the effect of stray radiation on observational data.

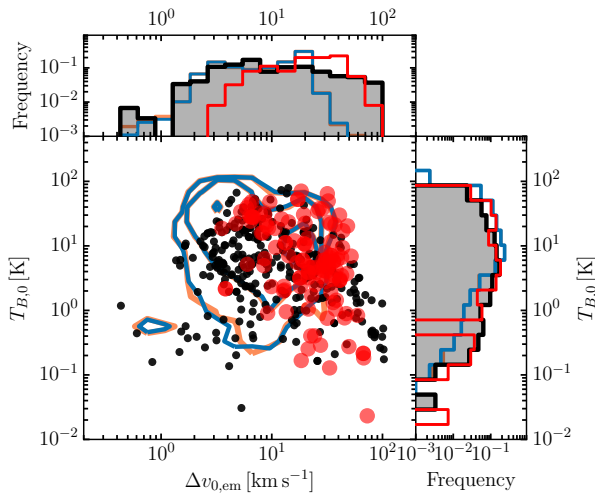


FIG. 18.— Parameters of Gaussian components ($\Delta v_{0,\text{em}}$, $T_{B,0}$) fitted by AGD to HI emission spectra from 21-SPONGE (black) and KOK14 synthetic observations including the WF effect (blue) and without the WF effect (orange). Contours indicate the 1, 2, and 3σ limits for the KOK14 distribution. We also include the AGD decomposition of HI emission spectra in the direction of the 21-SPONGE sources from the Leiden Argentine Bonn (LAB) survey (Kalberla et al. 2005) in red.